INTERNATIONAL JOURNAL FOR NUMERICAL METHODS IN ENGINEERING
Int. J. Numer. Meth. Engng 2005; **64**:1166–1206
Published online 14 June 2005 in Wiley InterScience (www.interscience.wiley.com). DOI: 10.1002/nme.1389

A finite-strain quadrilateral shell element based on discrete Kirchhoff–Love constraints

Pedro M. A. Areias, Jeong-Hoon Song and Ted Belytschko*,†

Department of Mechanical Engineering, Northwestern University, 2145 Sheridan Road, Evanston, IL 60208-3111, U.S.A.

SUMMARY

This paper improves the 16 degrees-of-freedom quadrilateral shell element based on pointwise Kirchhoff–Love constraints and introduces a consistent large strain formulation for this element. The model is based on classical shell kinematics combined with continuum constitutive laws. The resulting element is valid for large rotations and displacements. The degrees-of-freedom are the displacements at the corner nodes and one rotation at each mid-side node. The formulation is free of enhancements, it is almost fully integrated and is found to be immune to locking or unstable modes. The patch test is satisfied. In addition, the formulation is simple and amenable to efficient incorporation in large-scale codes as no internal degrees-of-freedom are employed, and the overall calculations are very efficient. Results are presented for linear and non-linear problems. Copyright © 2005 John Wiley & Sons, Ltd.

KEY WORDS: shell element; Kirchhoff–Love constraints; shear energy

1. INTRODUCTION

Shell element research in the past decades, with a few exceptions, has focused on shear-deformable elements, i.e. those based on variants of Mindlin/Reissner *plate* theory (e.g. References [1–5]). Although these elements have the advantage of being able to account for the transverse shear that occurs for thicker shells, low order forms of these elements are subject to shear locking. The amelioration of shear locking by auxiliary fields, such as in mixed elements and assumed strain elements, can lead to instabilities in the shear field. It is noteworthy that none of the 4-node quadrilaterals has yet been shown to meet the Babuska–Brezzi stability condition for arbitrary meshes.

*Correspondence to: Ted Belytschko, Department of Mechanical Engineering, Northwestern University, 2145 Sheridan Road, Evanston, IL 60208-3111, U.S.A.
†E-mail: tedbelytschko@northwestern.edu

Contract/grant sponsor: Office of Naval Research

Received 16 December 2004
Revised 3 March 2005
Accepted 18 April 2005

Despite the wide availability of established numerical formulations, two aspects remain unsatisfactory in the authors perspective. One is the frequent lack of an underlying classical shell theory (e.g. a physical model) supporting the numerical method (a fact identified by Simo *et al.* [6, 7]), and the lack of a simultaneously efficient and robust *quadrilateral* element formulation. For example, most quadrilateral elements show severe performance degradation for distorted meshes (c.f. Reference [8]). A difficulty with the commonly adopted degenerated continuum shell element framework of Ahmad *et al.* [1] is that shear (and membrane) locking occurs in its pristine form. In response to the inherent difficulties of treating thin shells, a variety of techniques has been developed over the years, such as reduced integration [9, 10], selective reduced integration [11] and its recent variants [12, 13], projection schemes [5, 14], assumed natural strain methods [15], enhanced strain methods [16], discrete shear gap methods [17], to mention just a few. We will not describe the historical details, as the reader can consult review articles (e.g. Reference [18]).

In this paper an improved element of the discrete-Kirchhoff genus, with long roots in the history of finite elements (see Reference [19]), is presented with the generalization for finite strains in the framework of a classical shell theory.

Existing shell theories are either based on three-dimensional continuum models with approximations permitted by the thickness, or *ab initio* two-dimensional models; Reference [20] discusses these classical approaches. Recently, it was found (c.f. Reference [21]) that the 'degenerated approach' by Ahmad *et al.* corresponds to a particular shell theory (not considered by classical studies such as Reference [20]).

As the main source of element complexity is related with the various required techniques developed to attenuate shear locking in shear-deformable shells, we avoid it. If the Kirchhoff–Love (KL) constraints are employed, there is no transverse shear energy and hence no shear locking occurs. However, it is well known that the finite element implementation of this theory with irreducible formulations requires high order elements and is far from simple (Reference [22] discusses these aspects).

The discrete-Kirchhoff (non-conforming) elements deal with this constraint at a specified number of points and allow low order interpolation to be used (e.g. References [23–25]). Of particular interest here is the configuration with mid-side rotations (e.g. References [19, 26, 27]). The semiloof element of Irons [28] is similar, but employs more nodes. The idea of using a *quadrilateral plate* with this configuration originates in the work of Fraejis de Veubeke [19] (Herrmann [24] proposed the use of 'crossed-triangles' to form a quadrilateral). It was later extended by Nagtegaal and Slater [29], Batoz *et al.* [25] and Crisfield and Tan [30]. The use of mid-side rotations is of paramount importance for our current work as in a recent attempt to extend our methodology for crack propagation in shells (inaugurated in Reference [31]) to folded geometries, we found that nodal spin degrees-of-freedom presented difficulties with the extended finite element method (XFEM). Elements with mid-side rotations can be easily incorporated within an XFEM framework, as will be seen in a subsequent paper.

Most previous work in *shells* with mid-side rotations was employed either triangles [24, 27, 32, 33] or *planar* quadrilaterals [25, 34], often under very restrictive assumptions (e.g. Reference [30]) such as moderate rotations and co-rotational formulations based on the super-position of a plane element with a plate bending element, valid for triangular elements only. Non-symmetric shape functions are employed in References [29, 35]. No complete theory, including the constraints, has been developed for them in the fully non-linear range. Despite these defects, the 'side rotation' degrees-of-freedom are very attractive for the aforementioned

reasons. Certain authors refer to difficulties of dealing with warped quadrilaterals with this formulation (c.f. Reference [34]), and these are required to solve most shell problems (e.g. most non-linear shell bending problems involve warping).

In light of the above, and while recognizing some advantages in the continuum-based shell models, we propose here a consistent thin-shell element based on discrete KL constraints and a thin shell theory. Curvilinear co-ordinates are used and the KL constraints are imposed at the sides of the element. Compared with co-rotational approaches (e.g. Reference [30]), the resulting equations are concise and transparent.

The proposed element degrees-of-freedom are mid-side rotations and nodal displacements, a nodal arrangement previously used in References [19, 25, 29, 30, 34]. Although the nodal arrangement is identical, the element is different from these developments in the general derivations and, in particular, its director shape functions and numerical quadrature. The proposed element makes *no* use of enhanced strain degrees-of-freedom or assumed strain fields, and is directly formulated, but it does use a special quadrature rule. During numerical testing, we obtained very accurate results in most tests.

The paper is organized as follows: In Section 2 we describe our shell model and explore some properties used in the following sections. In Section 3 we describe the quadrilateral discretization, and in particular the nodal arrangement and a pragmatical approach to co-ordinate transformation that avoids Lagrange multipliers. In Section 4 we inspect the performance of the element through a series of relevant tests and examples which show remarkable robustness and accuracy. Finally, Section 5 presents some conclusions and discusses the extensions in the works.

2. SHELL MODEL

2.1. Preliminary considerations

The shell theory we choose is characterized by the following:

- It obeys the KL strain constraints (c.f. Reference [36]).
- The form of the strain energy function is a particular case of the continuum strain energy density.
- Curvilinear co-ordinates are employed.
- Under KL constraints, transverse shear and normal stress components cannot be determined by constitutive considerations, as they are Lagrange multipliers. These are not explicitly obtained from weak equilibrium considerations either.

This model is a compromise between the continuum-based shell and classical shell theory. From the classical shell theory we retain the convenience of decoupled energies and the kinematic assumptions (see, e.g. References [20, 37]), and from the continuum description we make use of the generality provided by a specific form of the continuum strain energy. The latter is of special importance because diverse continuum constitutive equations can be incorporated in the existing shell framework with minimal alterations.

2.2. Undeformed geometry and KL constraints

The shell, whose undeformed region in $\mathbf{E}^3$ (the Euclidean 3-space) is here denoted as $\mathbf{\Omega}_0$, can be described by a reference surface $\mathscr{S}_0$, on which two curvilinear co-ordinates, θ^1 and θ^2, are

defined. The signed distance to the reference surface is denoted by a third (normal) curvilinear co-ordinate θ^3.

We make use the established convention for Latin and Greek indices (i.e. $i=1,2,3$; $\alpha=1,2$). If $\mathbf{n}_0(\theta^\alpha)$ represents the unitary normal to $\mathscr{S}_0$ and $\mathbf{R}(\theta^\alpha)$ represents the position of an arbitrary point on $\mathscr{S}_0$, then, for sufficiently large radius of curvature, any point $X \in \Omega_0$ is uniquely identified in the undeformed configuration according to its reference position

$$\mathbf{X}(\theta^i) = \mathbf{R}(\theta^\alpha) + \theta^3 \mathbf{n}_0(\theta^\alpha) \tag{1}$$

The applicability of (1) to a neighbourhood of any point in $\mathscr{S}_0$ is based on the assumption that points in this neighbourhood lie along one and only one normal to $\mathscr{S}_0$ (this is further discussed in Reference [20], where $\{\theta^i\}$ is said to form the 'normal' co-ordinate system). With the parametrization (1) we can directly write the particular forms of tangents, metric tensors and related quantities for the undeformed geometry of the shell Ω_0. We make use of the notation where a comma denotes a derivative with respect to the curvilinear co-ordinates (c.f. References [20, 36]). The first fundamental form of $\mathscr{S}_0$ is written as $A_{\alpha\beta} = \mathbf{R}_{,\alpha} \cdot \mathbf{R}_{,\beta}$ and the second fundamental form is written as $B_{\alpha\beta} = \mathbf{R}_{,\alpha\beta} \cdot \mathbf{n}_0 = -\mathbf{R}_{,\alpha} \cdot \mathbf{n}_{0,\beta}$. Note that neither $B_{\alpha\beta}$ nor $A_{\alpha\beta}$ depend on θ^3.

The curvilinear co-ordinates (θ^α) are such that $\mathbf{R}_{,\alpha}$ form a basis for the tangent space in $X \in \mathscr{S}_0$. For arbitrary θ^3, we define a family of surfaces $\mathscr{S}_0(\theta^3)$ with $\mathscr{S}_0(0) = \mathscr{S}_0$ for which the tangent basis is established from (1) as $\mathbf{X}_{,\alpha} = \mathbf{R}_{,\alpha} + \theta^3 \mathbf{n}_{0,\alpha}$. If we extend this basis by including $\mathbf{n}_0 = \mathbf{X}_{,3}$, the resulting basis spans Ω_0, and we can then define the metric of Ω_0 as $G_{ij} = \mathbf{X}_{,i} \cdot \mathbf{X}_{,j}$. The dual basis is given by $\mathbf{G}^i = G^{ij}\mathbf{X}_{,j}$ with $[G^{ij}] = [G_{ij}]^{-1}$.

Let us now inspect what occurs if $\mathscr{S}_0$ is deformed into a distinct surface $\mathscr{S}$. Let $\mathbf{x}$ denote the deformed counterpart of $\mathbf{X}$. Making use of lower-case notation for quantities defined in the deformed configuration of the shell, we can define the right Cauchy–Green tensor according to its components

$$\mathbf{C} = \mathbf{F}^{\mathrm{T}}\mathbf{F} = \underbrace{(\mathbf{x}_{,i} \cdot \mathbf{x}_{,j})}_{C_{ij}} \mathbf{G}^i \otimes \mathbf{G}^j \tag{2}$$

If the KL constraint holds, C_{ij}, and hence $\mathbf{C}$, are not arbitrary but obey the relation

$$C_{i3} = \delta_{i3} \tag{3}$$

Despite the apparent simplicity of (3), its consequences are far-reaching, because of the requirement that the compatibility conditions be satisfied (see the illuminating exposition in Reference [36]). The condition $C_{33} = 1$ is of special importance in this theory, and under this condition, no thickness change due to deformation occurs. We note that, in certain finite element implementations for rubber analysis [38], the thickness is forced to change due to the incompressibility condition, but the present shell *model*, in this form, is not suitable for such applications. However, this is not a limitation of the finite element application, and the proposed element could be modified to account for thickness changes (relaxing $C_{33} = 1$ in the *model*).

We opt, in contrast with our previous work [31], to make use of Naghdi shell theory [20]. This option opens the path to constructing modern shell theories including discontinuities under a firm theoretical framework.

Classical theories of deformable shells were developed as specialized cases of general elasticity, from which analytical studies could be done more conveniently. Shell theories make

use of known results of geometry concerning a Riemannian subspace (see References [39, 40]) together with the notion of thickness and both kinematical and constitutive assumptions. These are the crucial aspects of the shell theory and limit its applicability. We choose to avoid for now discussions on modern shell theories, and the interested reader is directed to the book edited by Fortin [41].

2.3. Stress and virtual work

Let s^{ij} represent the contra-variant scalar components of the Kirchhoff stress tensor (in the basis $\mathbf{x}_{,i} \otimes \mathbf{x}_{,j}$) and of the second Piola–Kirchhoff stress tensor (in the basis $\mathbf{X}_{,i} \otimes \mathbf{X}_{,j}$). The virtual work of the internal forces can be written in terms of a kinematically admissible position change, i.e. $\delta\mathbf{x}$. Because $C_{i3} = \delta_{i3}$, it follows that $\delta C_{i3} = 0$. If $\sqrt{G} = [\mathbf{G}_1 \cdot (\mathbf{G}_2 \times \mathbf{G}_3)] > 0$ then the work of internal forces, δW_{I} can be written as

$$\delta W_{\mathrm{I}} = \int_V s^{\alpha\beta} \mathbf{x}_{,\beta} \cdot \delta\mathbf{x}_{,\alpha} \sqrt{G}\, \mathrm{d}\theta^1\, \mathrm{d}\theta^2\, \mathrm{d}\theta^3 \tag{4}$$

and, denoting as δW_{E} the work of imposed forces, the weak form of the equilibrium equations follows as

$$\delta W_{\mathrm{I}} = \delta W_{\mathrm{E}} \tag{5}$$

Note that s^{i3}, s^{33} and s^{3i} are not necessarily zero, but rather do not contribute to the internal work. As will be seen later, they are Lagrange multipliers for the KL constraints. By means of (2) of we can write (5) as

$$\int_V s^{\alpha\beta} [(\mathbf{r}_{,\alpha} + \theta^3 \mathbf{n}_{,\alpha}) \delta\mathbf{r}_{,\beta} + \theta^3 (\mathbf{r}_{,\alpha} + \theta^3 \mathbf{n}_{,\alpha}) \delta\mathbf{n}_{,\beta}] \sqrt{G}\, \mathrm{d}\theta^1\, \mathrm{d}\theta^2\, \mathrm{d}\theta^3 = \delta W_{\mathrm{E}} \tag{6}$$

Traditionally, the variables $\mathbf{x}_{,\alpha}$, $\delta\mathbf{x}_{,\beta}$ and $s^{\alpha\beta}$ in (4) are specialized by making use of the deformed second fundamental form, as $\mathbf{n}$ is still a unitary normal vector in the KL theory. However, we retain the term $\mathbf{n}_{,\alpha}$ in (6), despite taking advantage of the KL simplifications. We do not use stress resultants as in classical derivations [20]. Note that we retain all terms and make no simplifications beyond our initial assumptions (3). Assuming a 'linearized' version of the *continuum* constitutive law and (local) plane stress, we can write

$$s^{\alpha\beta} = E^{\alpha\beta\gamma\eta} \varepsilon_{\gamma\eta} \tag{7}$$

where $\varepsilon_{\gamma\eta}$ are the covariant components of the Green–Lagrange strain tensor. These are given by

$$\begin{aligned} \varepsilon_{\gamma\eta} &= \tfrac{1}{2}(\mathbf{x}_{,\gamma} \cdot \mathbf{x}_{,\eta} - \mathbf{X}_{,\gamma} \cdot \mathbf{X}_{,\eta}) \\ &= \tfrac{1}{2}[a_{\gamma\eta} - A_{\gamma\eta} - 2\theta^3 (b_{\eta\gamma} - B_{\gamma\eta}) + (\theta^3)^2 (\mathbf{n}_{,\gamma} \cdot \mathbf{n}_{,\eta} - \mathbf{n}_{0,\gamma} \cdot \mathbf{n}_{0,\eta})] \end{aligned} \tag{8}$$

where the explicit strain dependence upon θ^3 and $(\theta^3)^2$ is apparent. Note that symmetry of the fundamental forms was used in obtaining (8).

We will consider isotropic elastic materials (although this is not a limitation of the model) with the elasticity coefficients $E^{\alpha\beta\gamma\eta}$ assumed to be constant (in the material frame), and dependent on Young's modulus E and Poisson coefficient ν, according to

$$E^{\alpha\beta\gamma\eta} = \frac{E}{2(1+\nu)}\left(G^{\alpha\gamma}G^{\beta\eta} + G^{\alpha\eta}G^{\beta\gamma} + \frac{2\nu}{1-\nu}G^{\alpha\beta}G^{\gamma\eta}\right) \tag{9}$$

with $[G^{\alpha\beta}] = [G_{\alpha\beta}]^{-1} = [\mathbf{X}_{,\alpha}\cdot\mathbf{X}_{,\beta}]^{-1}$. In Equation (6) the classical relations between the derivatives of the normal (director) vector and the tangents are not introduced yet. These are included by means of Lagrange multiplier fields, but in an unconventional manner. We do not impose all $C_{i3} = \delta_i^3$ through s^{i3}. The director inextensibility, which is imposed by use of spherical co-ordinates as described later, eliminates the presence of s^{33} (e.g. it is imposed by the use of a 'co-ordinate transformation technique'). Therefore, we add the terms corresponding to the Lagrange multipliers $s^{\alpha 3}$ which modify (6) into

$$\begin{aligned}\int_V s^{\alpha\beta}[&(\mathbf{r}_{,\alpha} + \theta^3\mathbf{n}_{,\alpha})\cdot\delta\mathbf{r}_{,\beta} + \theta^3(\mathbf{r}_{,\alpha} + \theta^3\mathbf{n}_{,\alpha})\cdot\delta\mathbf{n}_{,\beta}\\ &+ \delta s^{\alpha 3}(\mathbf{n}\cdot\mathbf{r}_{,\alpha}) + s^{\alpha 3}(\delta\mathbf{n}\cdot\mathbf{r}_{,\alpha} + \mathbf{n}\cdot\delta\mathbf{r}_{,\alpha})]\sqrt{G}\,\mathrm{d}\theta^1\,\mathrm{d}\theta^2\,\mathrm{d}\theta^3 = \delta W_{\mathrm{E}}\end{aligned} \tag{10}$$

The solution of (10) involves a Newton numerical scheme in which $\mathrm{d}\delta W_{\mathrm{I}}$, the first variation of δW_{I}, is needed. It is straightforward to show that $\mathrm{d}\delta W_{\mathrm{I}}$ can be written as

$$\begin{aligned}\mathrm{d}\delta W_{\mathrm{I}} = \int_V \{&s^{\alpha\beta}[(\mathrm{d}\mathbf{r}_{,\alpha} + \theta^3\,\mathrm{d}\mathbf{n}_{,\alpha})(\delta\mathbf{r}_{,\beta} + \theta^3\delta\mathbf{n}_{,\beta}) + (\mathbf{r}_{,\alpha} + \theta^3\mathbf{n}_{,\alpha})(\mathrm{d}\delta\mathbf{r}_{,\beta} + \theta^3\,\mathrm{d}\delta\mathbf{n}_{,\beta})]\\ &+ E^{\alpha\beta\gamma\eta}[(\mathbf{r}_{,\alpha} + \theta^3\mathbf{n}_{,\alpha})(\delta\mathbf{r}_{,\beta} + \theta^3\delta\mathbf{n}_{,\beta})][(\mathbf{r}_{,\gamma} + \theta^3\mathbf{n}_{,\gamma})(\mathrm{d}\mathbf{r}_{,\eta} + \theta^3\,\mathrm{d}\mathbf{n}_{,\eta})]\\ &+ \delta s^{\alpha 3}(\mathrm{d}\mathbf{n}\cdot\mathbf{r}_{,\alpha} + \mathbf{n}\cdot\mathrm{d}\mathbf{r}_{,\alpha}) + \mathrm{d}s^{\alpha 3}(\delta\mathbf{n}\cdot\mathbf{r}_{,\alpha} + \mathbf{n}\cdot\delta\mathbf{r}_{,\alpha})\\ &+ s^{\alpha 3}(\mathrm{d}\delta\mathbf{n}\cdot\mathbf{r}_{,\alpha} + \mathrm{d}\mathbf{n}\cdot\delta\mathbf{r}_{,\alpha}) + s^{\alpha 3}(\delta\mathbf{n}\cdot\mathrm{d}\mathbf{r}_{,\alpha} + \mathbf{n}\cdot\mathrm{d}\delta\mathbf{r}_{,\alpha})\}\sqrt{G}\,\mathrm{d}\theta^1\,\mathrm{d}\theta^2\,\mathrm{d}\theta^3\end{aligned} \tag{11}$$

Any specific implementation depends on the approximation of the variables $\mathbf{r}$, $\mathbf{n}$ and their first and second variations. A convenient basis in the shell geometry should be chosen first. This is generally a matter of convenience, and we have already specified an elastic law in a material basis and also specified the KL condition in terms of these components. After the *components* are specified, it seems natural to use the basis $\mathbf{R}_{,\alpha}$. Note that some authors prefer the use of the basis $(\mathbf{r}_{,\alpha})$.

Some of the terms in Equation (11) deserve special attention. For example the term $\mathrm{d}\delta\mathbf{n}$ arises from the fact that the condition $\mathbf{n}\cdot\mathbf{r}_{,\alpha} = 0$ can be imposed either through the Lagrange multipliers $s^{\alpha 3}$ or through a specific relation between $\mathbf{n}$ and $\mathbf{r}$ so that, in the latter, the terms naturally vanish, in agreement with what occurs with the condition $\mathbf{n}\cdot\mathbf{n} = 1$ if spherical co-ordinates are employed in the definition of $\mathbf{n}$.

In what follows, we opt to use distinct interpolation functions for mid-side rotations and for nodal positions and displacements. The discrete version of the KL conditions is detailed in the following sections.

3. FINITE ELEMENT DISCRETIZATION

3.1. Element characteristics

Our particular quadrilateral element is characterized by a number of specificities, itemized below:

- Thickness is assumed to be uniform.
- Four corner nodes for position and displacement interpolation are employed.
- Four mid-side rotations are employed.
- A special quadrature is employed for both membrane and bending terms.
- Director shape functions are *newly* developed, characterized by the absence of non-symmetric terms (see previous developments [29, 30, 35]).

The kinematic relations and weak form of equilibrium follow the results of the previous section, and the above specificities.

3.2. Shape functions, director interpolation and numerical quadrature

The shell model of the previous section is implemented using the element depicted in Figure 1 (represented in a deformed configuration). For conciseness, the nomenclature of the previous section is extended to the finite element context. Variables defined in the reference configuration are identified by the same symbols, but uppercase is adopted.

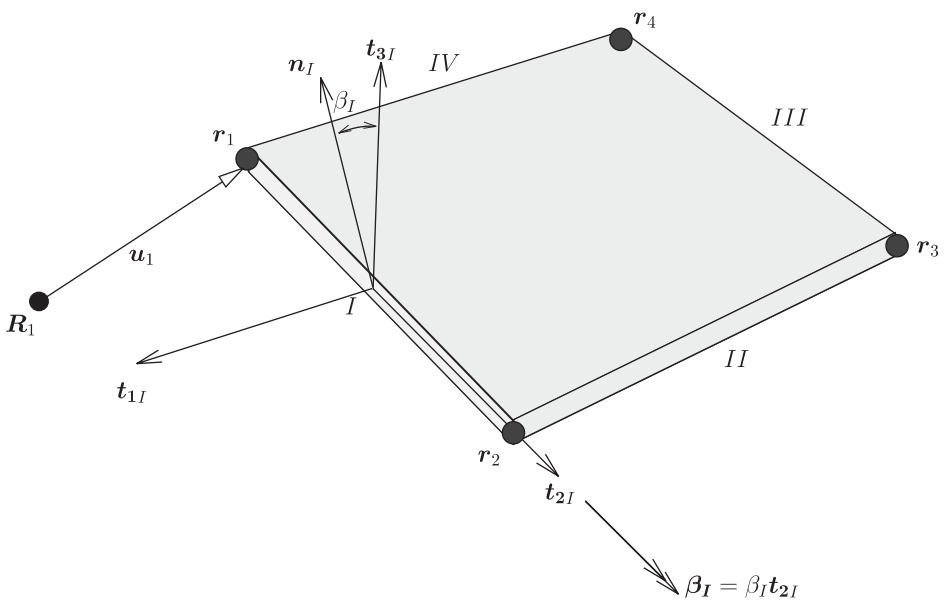

Figure 1. Deformed configuration of a typical shell element. Only the degrees-of-freedom of node 1 ($\mathbf{u}_1$) and side I (β_I) are depicted.

The deformed mid-surface position, $\mathbf{r}(\theta^1, \theta^2)$ is interpolated using conventional bi-linear shape functions $N_K(\theta^1, \theta^2)$, where $(\theta^1, \theta^2) \in [-1, 1] \times [-1, 1]$:

$$\mathbf{r}(\theta^1, \theta^2) = \sum_{K=1}^{4} N_K(\theta^1, \theta^2)\mathbf{r}_K = \sum_{K=1}^{4} \frac{1}{4}(1 + \theta^1\theta^{1K})(1 + \theta^2\theta^{2K})\mathbf{r}_K \tag{12}$$

where K represents the corner node number $(K = 1, \ldots, 4)$ and θ^{iK} are the values of the curvilinear co-ordinates θ^i evaluated at nodes K. The reference mid-surface position, $\mathbf{R}(\theta^1, \theta^2)$ is obtained by the same discretization.

The interpolation for the deformed director field $\mathbf{n}$ depends in the directors at the mid-side values $\mathbf{n}_P$, with $P = \mathrm{I}, \mathrm{II}, \mathrm{III}, \mathrm{IV}$:

$$\mathbf{n}(\theta^1, \theta^2) = \sum_{P=I}^{\mathrm{IV}} M_P(\theta^1, \theta^2)\mathbf{n}_P \tag{13}$$

with an analogous interpolation for the reference director field, $\mathbf{n}_0$.

The shape functions $M_P(\theta^1, \theta^2)$ in (13) are distinct from the ones employed in (12). We also use shape functions with quadratic terms, but they are different from those in References [29, 30] (note that Batoz *et al.* favour the so-called 'rational' shape functions [25]). In References [30, 35], a central node was considered in the derivation of the shape functions, which did not possess the usual spatial symmetries. In addition, those authors took other special steps in the derivations, including the introduction of two parameters to satisfy the patch test. For a general warped mid-surface, these parameters were approximately determined using a 'planified element' [30]. This, along with the aforementioned non-symmetric shape functions, may have been the obstacles to the widespread use of this element type, and are here removed. It is noted that, in these works, a connection between the central degrees-of-freedom and the mid-side degrees-of-freedom is carried out, with more than one possibility to accomplish this task. We circumvent these considerations and procedures by starting with a complete quadratic polynomial for each mid-side node shape function and by imposing the unitary sum condition, the symmetry conditions, the exact representation of a linear director field and the exact representation of a side average director. We do not make use of a central node or planification of warped elements. The difficulty of meeting the patch test, which required planar elements in References [25, 34] and approximate techniques in Reference [30], is here avoided by a specific quadrature scheme.

For the purpose of defining the director shape functions, let us start with a general quadratic polynomial for each director shape function $M_P(\theta^1, \theta^2)$:

$$M_P(\theta^1, \theta^2) = a_P + b_P\theta^1 + c_P\theta^2 + d_P\theta^1\theta^2 + e_P(\theta^1)^2 + f_P(\theta^2)^2 \tag{14}$$

where $a_P, \ldots, f_P$ are polynomial coefficients corresponding to each mid-side node $P = \mathrm{I}, \ldots, \mathrm{IV}$.

Symmetry requirements (Nagtegaal and Slater [29] and Crisfield and Tan [35] did not require their shape functions to be symmetric) result in the following relations:

- $a_1 = a_2 = a_3 = a_4 = a$
- $b_1 = c_2 = -b_3 = -c_4 = b$
- $c_1 = -b_2 = -c_3 = b_4 = c$
- $d_1 = d_2 = d_3 = d_4 = d = 0$

- $e_1 = f_2 = e_3 = f_4 = e$
- $f_1 = e_2 = f_3 = e_4 = f$

with $a, \ldots, f$ being new shape function coefficients. The cross-term coefficients d_P must be null for symmetry of the shape functions. These terms had a role in the original derivations in References [29, 30], related with the reproduction of an affine *rotation* field. Our formulation reproduces exactly an affine *director* field, due to the quadrature rule employed. If rotations are small enough, then the representation of an affine director field coincides with the requirement for representing an affine rotation field.

Introducing the condition of unitary sum of the shape functions, $\sum_{P=I}^{\mathrm{IV}} M_P(\theta^1, \theta^2) = 1$, we obtain the additional equalities:

- $a = \frac{1}{4}$
- $e = -f$

Therefore, it remains to calculate b, c and e. This task can be easily carried out using the equality relation between the average director along a side and the mid-side director. In this circumstance, the coefficients b, c and e are

- $b = 0$
- $c = -\frac{1}{2}$
- $e = -\frac{3}{8}$

We can finally write the (mid-side) director shape functions as

$$M_P(\theta^1, \theta^2) = \tfrac{1}{4} + \tfrac{3}{8}(\theta^{2P})^2[(\theta^2)^2 - (\theta^1)^2] + \tfrac{1}{2}\,\theta^{2P}\theta^2 + \tfrac{3}{8}(\theta^{1P})^2[(\theta^1)^2 - (\theta^2)^2] + \tfrac{1}{2}\theta^{1P}\theta^1 \quad (15)$$

where, in agreement with what was done for the corner nodes shape functions, we employ the notation θ^{iP} to identify the ith curvilinear co-ordinate value of mid-side node P.

We now show that if an affine director field is imposed, it is exactly represented whenever $\theta^1\theta^2 = 0$. Let $\mathbf{n}^*(\mathbf{x})$ denote an affine director field, which can be written as ($\mathbf{r}$ is the mid-surface displacement)

$$\mathbf{n}^*(\mathbf{r}) = \mathbf{n}_0^* + \mathbf{A}\mathbf{r} \quad (16)$$

with $\mathbf{n}_0^*$ being a given constant vector and $\mathbf{A}$ a constant, but otherwise generic 3×3 matrix.

Using (16) and (15), we write

$$\mathbf{n}_0^* + \mathbf{A}\mathbf{r} = \sum_{P=I}^{\mathrm{IV}} M_P \mathbf{n}_0^* + \mathbf{A} \sum_{P=I}^{\mathrm{IV}} M_P \mathbf{r}_P \quad (17)$$

where $\mathbf{r}_P$ denote the values of $\mathbf{r}$ at the mid-side nodes.

It is clear that the first term in the left-hand side of (17) has the same value as the first term in the right-hand side. It remains to show that, if $\mathbf{r} = \sum_{K=1}^{4} N_K \mathbf{r}_K$, then, for arbitrary $\mathbf{A}$,

$$\sum_{K=1}^{4} N_K \mathbf{r}_K = \sum_{P=I}^{\mathrm{IV}} M_P \mathbf{r}_P \quad (18)$$

must hold for all quadrature points. Because $\mathbf{r}_K$ are assumed to be arbitrary, we must inspect each term of (18).

For the constant term, we have $\mathbf{r}_{\mathrm{I}}+\mathbf{r}_{\mathrm{II}}+\mathbf{r}_{\mathrm{III}}+\mathbf{r}_{\mathrm{IV}}=\mathbf{r}_1+\mathbf{r}_2+\mathbf{r}_3+\mathbf{r}_4$, for the linear term in θ^1 we have $\theta^1\{(\mathbf{r}_{\mathrm{IV}}-\mathbf{r}_{\mathrm{II}})+\frac{1}{2}[\mathbf{r}_2+\mathbf{r}_3-(\mathbf{r}_1+\mathbf{r}_4)]\}=0$ and for the linear term in θ^2 we have $\theta^2\{(\mathbf{r}_{\mathrm{III}}-\mathbf{r}_{\mathrm{I}})+\frac{1}{2}[\mathbf{r}_1+\mathbf{r}_2-(\mathbf{r}_3+\mathbf{r}_4)]\}=0$. The two quadratic terms also vanish identically, with $\frac{3}{8}(\theta^1)^2(\mathbf{r}_{\mathrm{I}}+\mathbf{r}_{\mathrm{III}}-\mathbf{r}_{\mathrm{II}}-\mathbf{r}_{\mathrm{IV}})=0$ and $\frac{3}{8}(\theta^2)^2(\mathbf{r}_{\mathrm{I}}+\mathbf{r}_{\mathrm{III}}-\mathbf{r}_{\mathrm{II}}-\mathbf{r}_{\mathrm{IV}})=0$.

We note that the bi-linear term is problematic, because we have the requirement that $\theta^1\theta^2[\mathbf{r}_1+\mathbf{r}_3-(\mathbf{r}_2+\mathbf{r}_4)]=0$. It is possible to conclude that the bi-linear term vanishes only if (at least) one of the following conditions holds:

1. $\theta^1=0$ or $\theta^2=0$.
2. The element is a parallelogram.

Our approach to this problem consists in using a quadrature rule that satisfies condition 1. The idea consists in using a $2\times 2+1$ cross-shaped quadrature point distribution, as shown in Figure 2. A 4-point variant of this quadrature rule was employed, using a triangular subdivision of the quadrilateral, in the context of plane quadrilateral membrane elements, by Reddy and Küssner [42]. It was found, in that context, to be beneficial in terms of element performance, when compared with the usual Gauss quadrature. We used our quadrature with success in all examples of this paper. It is worth mentioning that this scheme is not required for the bending terms, but for the sake of generality (decoupling of bending and membrane strain energy is not possible for general constitutive models), all terms are integrated as indicated in Figure 2. For the points along the θ^3 direction, we use standard 2-point Gauss quadrature.

The rationale for the weights and positions is as follows. We start with a quartic polynomial in θ^1 and θ^2 and arrange 8 points distributed symmetrically on the two lines I–III and II–IV (see Figure 2). The distances between the quadrature points and the element's centre are denoted by l and k where $l<k$ and the respective weights are w_l and w_k. We readily conclude that such a scheme cannot integrate the $(\theta^1\theta^2)^2$ terms and further that the following indeterminate system holds for k, l, w_l and w_k:

$$\begin{aligned} k^4w_k+l^4w_l&=\tfrac{2}{5}\\ k^2w_k+l^2w_l&=\tfrac{2}{3}\\ w_k+w_l&=1 \end{aligned} \tag{19}$$

If we collapse the four *l-points* making $l=0$, we obtain a 5-*point* quadrature (in the plane case, this type of quadrature was used, for example, in Reference [43]).

From this point on, we extend the notation of the shape functions and all quantities identified with a P subscript are associated with mid-side nodes and, in contrast, quantities identified with a K subscript are associated with corner nodes. The same applies to the Arabic and Roman numerals (the former indicating a corner node number and the latter indicating a mid-side node).

3.3. KL conditions and discrete counterparts

It is well known that the use of spherical components for the definition of the director $\mathbf{n}$ circumvents the need for an explicit term with the stress component s^{33} in the weak (constrained) form of the equilibrium equations (e.g. Reference [44]). It is worth mentioning that the condition $C_{33}=1$ (and its discrete counterpart) is employed in other shell models *not*

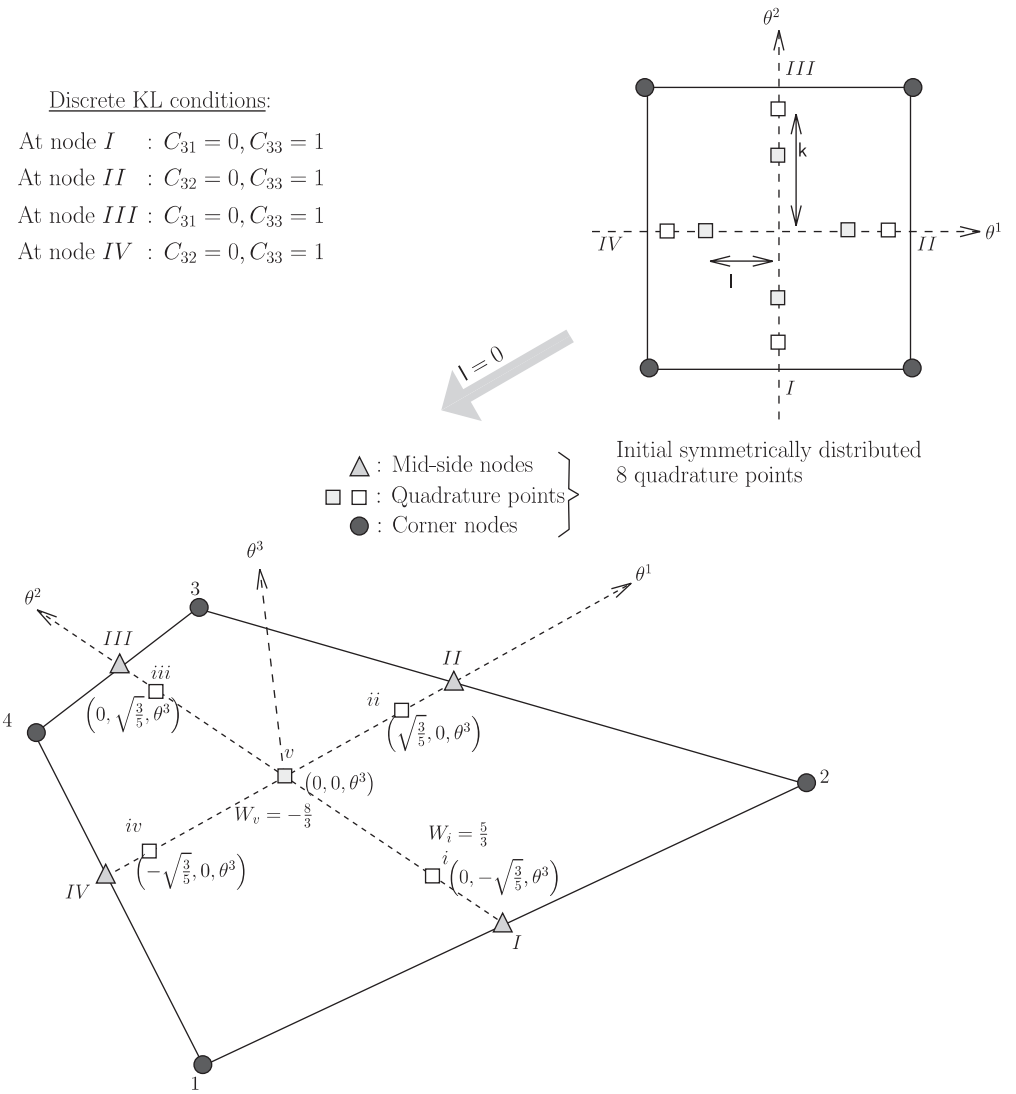

Figure 2. Quadrature scheme for a given θ^3. The quadrature point positions for $i,\ldots,v$ are given, and only the weights of quadrature points i and v are depicted. The KL conditions are imposed at the mid-side points $\mathrm{I},\ldots,\mathrm{IV}$ as listed.

based on the KL conditions. Many authors make use of the 'Rodrigues formula' (in recognition of the work of Olinde Rodrigues, see Reference [45] for a historical viewpoint on the man and the formula) to rotate the reference director field $\mathbf{n}_0$ to its deformed counterpart $\mathbf{n}$ using two (or three) Euler angles. It is clear that if $\|\mathbf{n}_0\|_2=1$ then this deformed director will also satisfy $\|\mathbf{n}\|_2=1$ without the explicit requirement for an s^{33} term. We will also incorporate the remaining conditions $C_{13}=0$ and $C_{23}=0$ through analogous transformations of the directors.

Despite the different contexts, an analogy can be made with the 'transformation methods' to impose equality conditions in constrained optimization.

If these KL conditions are met through transformation, it is clear that we can discard the Lagrange multipliers s^{3i}. Therefore, to impose $C_{13}=0$ and $C_{23}=0$ we use side rotations in the spirit of Morley [26], Dawe [27] in the triangle context. The idea consists in selecting specific points where $C_{13}=0$ is satisfied and $C_{23}=0$ is violated and vice-versa. In general, in each of the discrete-Kirchhoff points, either $C_{13}=0$ and $C_{33}=1$ are satisfied *or* $C_{23}=0$ and $C_{33}=1$ are satisfied. In contrast with previous works (e.g. Herrmann proposed 'crossed-triangles' [24] to form a quadrilateral), we have a true quadrilateral, which can be warped, and there are no limitations exists either on the rotation (i.e. bending) amplitude or membrane stretching. For conciseness, we do not present the complete details of the implementation, as adequate symbolic algebra systems are available to carry out the needed operations. We used such a system to generate Fortran code used in our implementation.

One should observe that no requirement exists for an averaged normal along each element's sides. This contrasts with established procedures (which define a common side normal), and it allows an arbitrary number of elements to share a common side. This versatility in treating corners and edges is not present in other finite strain formulations, including the ones using three nodal Euler angles. The validity of this technique rests on the fact that rigid body rotations rotate elements' normals[‡] by the same amount.

Considering the generic side I (see Figure 1) and its undeformed counterpart, the undeformed 'side triad' $\mathbf{T}_{LP}$ (corresponding to $\mathbf{t}_{lp}$ in Figure 1) at $P=I$ with $L=1,2,3$ and $\mathbf{n}_{0P}=\mathbf{T}_{3P}$ is given by

$$\mathbf{T}_{1I}=\mathbf{T}_{2I}\times\mathbf{T}_{3I} \tag{20a}$$

$$\mathbf{T}_{2I}=\frac{\mathbf{R}_2-\mathbf{R}_1}{\|\mathbf{R}_2-\mathbf{R}_1\|} \tag{20b}$$

$$\mathbf{T}_{3I}=\mathbf{n}_{0I}=\frac{\mathbf{T}'_{3I}}{\|\mathbf{T}'_{3I}\|}\quad\text{with }\mathbf{T}'_{3I}=\mathbf{T}_{2I}\times(\mathbf{R}_4+\mathbf{R}_3-\mathbf{R}_2-\mathbf{R}_1) \tag{20c}$$

For sides $P=\mathrm{II},\mathrm{III}$ and IV one can accordingly write the corresponding triads by a permutation of indices in (20). It is observed that the deformed side-vector corresponding to (20b) can be written as

$$\mathbf{t}_{2I}=\frac{\mathbf{r}_2-\mathbf{r}_1}{\|\mathbf{r}_2-\mathbf{r}_1\|} \tag{21}$$

Because both $\mathbf{t}_{2I}$ and $\mathbf{T}_{2I}$ are common to all elements sharing this side, it is possible to define normals for the shared side of each element, based solely on the undeformed normal $(\mathbf{T}_{3I})$ and the two side-vectors ($\mathbf{T}_{2I}$ and $\mathbf{t}_{2I}$)

$$\mathbf{t}_{3I}=\mathbf{\Lambda}(\mathbf{T}_{2I},\mathbf{t}_{2I})\mathbf{T}_{3I} \tag{22}$$

[‡]Keep in mind that, in the discrete setting under the KL conditions, directors and normals are distinct vectors.

where the rotation matrix $\mathbf{\Lambda}(\mathbf{T}_{2I}, \mathbf{t}_{2I})$ takes a specific form of the general case (see Reference [31])

$$\mathbf{\Lambda}(\mathbf{T}_{2I}, \mathbf{t}_{2I}) = \left[\mathbf{I} + \mathbf{S}(\mathbf{T}_{2I}, \mathbf{t}_{2I}) + \frac{1}{1 + \mathbf{T}_{2I} \cdot \mathbf{t}_{2I}} \mathbf{S}(\mathbf{T}_{2I}, \mathbf{t}_{2I})^2\right] \tag{23a}$$

where $\mathbf{S}(\mathbf{T}_{2I}, \mathbf{t}_{2I})$ is the following skew-symmetric matrix, written as a function of the scalar components of $\mathbf{t}_2$ and $\mathbf{T}_2$:

$$\mathbf{S}(\mathbf{T}_{2I}, \mathbf{t}_{2I}) = \begin{bmatrix} 0 & -T_{2I1}t_{2I2} + T_{2I2}t_{2I1} & T_{2I3}t_{2I1} - T_{2I1}t_{2I3} \\ T_{2I1}t_{2I2} - T_{2I2}t_{2I1} & 0 & -T_{2I2}t_{2I3} + T_{2I3}t_{2I2} \\ -T_{2I3}t_{2I1} + T_{2I1}t_{2I3} & T_{2I2}t_{2I3} - T_{2I3}t_{2I2} & 0 \end{bmatrix} \tag{23b}$$

where T_{2Ij} is the component j of $\mathbf{T}_{2I}$.

It is interesting to note that only the spin components along $\mathbf{t}_{2I} \times \mathbf{T}_{2I}$ matter in the definition of (22). The rotated normals contain the same amount of (spin) rotation for each element sharing the corresponding side.

Similar to (22), the vector $\mathbf{t}_{1I}$ is obtained as

$$\mathbf{t}_{1I} = \mathbf{\Lambda}(\mathbf{T}_{2I}, \mathbf{t}_{2I})\mathbf{T}_{1I} \tag{24}$$

Evidently, general rigid body rotations should include a component around $\mathbf{t}_{2I}$, besides the rotation of $\mathbf{t}_{2I}$ itself. The rotation vector around $\mathbf{t}_{2I}$ is indicated in Figure 1 as $\boldsymbol{\beta}_I$. Making use of this rotation vector, the mid-side director $\mathbf{n}_I$ is finally written as

$$\mathbf{n}_I = \mathbf{\Lambda}^*(\boldsymbol{\beta}_I)\mathbf{t}_{3I} = \mathbf{\Lambda}^*(\boldsymbol{\beta}_I)\mathbf{\Lambda}(\mathbf{T}_{2I}, \mathbf{t}_{2I})\mathbf{n}_{0I} \tag{25}$$

where $\mathbf{\Lambda}^*(\boldsymbol{\beta}_I)$ is the standard rotation matrix (c.f. Reference [31]).

In general, for a given mid-side node P, the deformed normals $\mathbf{n}_P$ can be written as

$$\mathbf{n}_P = \cos(\beta_P)\mathbf{t}_{3P} + \sin(\beta_P)\mathbf{t}_{1P} \tag{26}$$

with β_P being the mid-side node P degrees-of-freedom.

A picture with a 2D (in this case $\mathbf{t}_{3I} = \mathbf{T}_{3I}$) interpretation of β_P as a rigid body degrees-of-freedom is shown in Figure 3. Generally, the deformation is a combination of bending, stretching, and rigid body displacement.

One could use alternative definitions of (20); for example, when compared with the work of Crisfield *et al.* [30, 32, 33] we do not impose a common side normal to adjacent elements. Our definition of the side triad (20) is not arbitrary but guarantees compatibility of side rotation for elements sharing the same side, whether they are co-planar or not.

In the plane, elements can have counter-clockwise or clockwise nodal numbering. It should be noted that in the assembly of the rotation degrees-of-freedom, the global node numbering is used to introduce a global orientation to each side.

With this methodology, the discrete counterpart of the condition $C_{13} = 0$ is imposed in the sides $\theta^2 = \pm 1$ and $C_{23} = 0$ is imposed in the sides $\theta^1 = \pm 1$, as depicted in Figure 2. The condition $C_{33} = 1$ is imposed at all four sides through the use of polar co-ordinates in the four

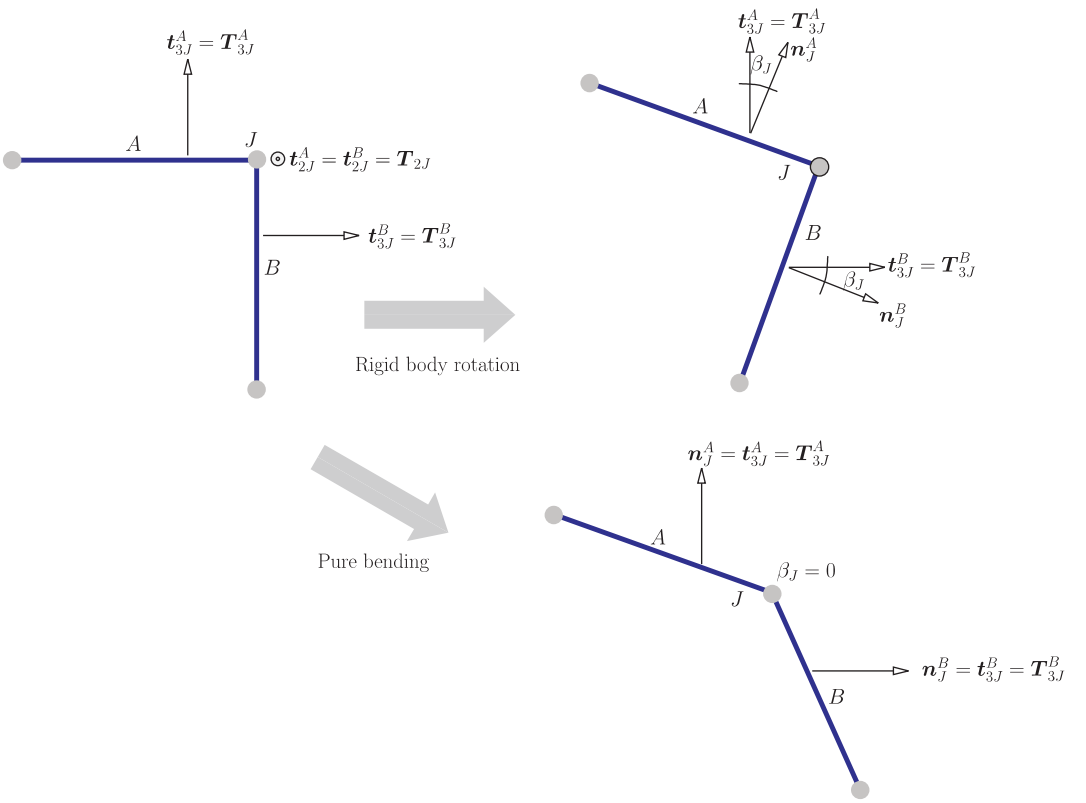

Figure 3. Interpretation of β_J as rigid body degrees-of-freedom. If pure-bending occurs (around $\mathbf{T}_{2J}$) then $\beta_J = 0$. In general, the motion is a combination of the two depicted situations.

planes defined by the side-vectors $\mathbf{t}_{3P}$ and $\mathbf{t}_{1P}$. This particular arrangement is not unique and other forms could be explored in future works.

3.4. Discretization of the constrained director and equilibrium equations

The entire finite element formulation is expressed in terms of the fields $\mathbf{n}$, $\mathbf{r}$, their surface co-ordinate derivatives $\mathbf{n}_{,\alpha}$, $\mathbf{r}_{,\alpha}$ and respective first and second variations. The variables related to $\mathbf{r}_{,\alpha}$ involve a relatively simple discretization, following classical finite element derivations, and we briefly present the terms arising from $\mathbf{n}_{,\alpha}$.

We can write the director vector variation, $\mathbf{n}(\theta^1, \theta^2)$, omitting the explicit dependence upon θ^α, as

$$\delta\mathbf{n}_{,\alpha} = \sum_{P=I}^{\mathrm{IV}} \frac{\partial M_P}{\partial \theta^\alpha}\,\delta\mathbf{n}_P = \sum_{P=I}^{\mathrm{IV}} \mathbf{A}_{1P}\delta\beta_P + \sum_{P=I}^{\mathrm{IV}}\sum_{K=1}^{4} \mathbf{A}_{2PK}\cdot\delta\mathbf{r}_K \tag{27a}$$

where $\mathbf{A}_{1P}$ is a three-dimensional vector and $\mathbf{A}_{2PK}$ is a 3×3 matrix. An analogous expression for $\mathrm{d}\mathbf{n}_{,\alpha}$ follows from relation (27a).

The second variation of $\mathbf{n}_{,\alpha}$ can be written as

$$\mathrm{d}\delta\mathbf{n}_{,\alpha} = \sum_{P=I}^{\mathrm{IV}} \frac{\partial M_P}{\partial\theta^\alpha}\,\mathrm{d}\delta\mathbf{n}_P = \sum_{P=I}^{\mathrm{IV}} \mathbf{A}_{3P}\delta\beta_P\,\mathrm{d}\beta_P + \sum_{P=I}^{\mathrm{IV}}\sum_{K=1}^{4} \delta\beta_P\mathbf{A}_{4PK}\cdot\mathrm{d}\mathbf{r}_K$$

$$+ \sum_{P=I}^{\mathrm{IV}}\sum_{K=1}^{4} \mathrm{d}\beta_P\mathbf{A}_{5PK}\cdot\delta\mathbf{r}_K + \sum_{P=I}^{\mathrm{IV}}\sum_{K=1}^{4}\sum_{M=1}^{4} \delta\mathbf{r}_K\cdot\mathbf{A}_{6KPM}\cdot\mathrm{d}\mathbf{r}_M \tag{27b}$$

The arrays $\mathbf{A}_3,\ldots,\mathbf{A}_6$ were evaluated using symbolic algebra.

For the correct integration through the thickness, h, we must calculate, for each element, the domain of $\theta^3\in[\alpha,h+\alpha]$ with $\alpha<0$ (see Reference [20] for a discussion). This is accomplished by assuming that the undeformed mass density is uniform in the shell, and in particular along the thickness direction. Using Reference [20], the lower limit of θ^3 domain, α, is determined from the following equality:

$$\int_\alpha^{h+\alpha} \sqrt{G}\theta^3\,\mathrm{d}\theta^3 = 0 \tag{28}$$

To obtain a closed-form solution for α, we evaluate the left-hand side of (28) at $\theta^\alpha=0$. In this case, the structure of the undeformed co-variant basis is very interesting, and it uncovers an analogy with the formulas (20):

$$\mathbf{G}_{,1}(\mathbf{0},\theta^3) = \frac{1}{2}(\mathbf{R}_{\mathrm{II}}-\mathbf{R}_{\mathrm{IV}}) + \frac{\theta^3}{2}(\mathbf{n}_{0\mathrm{II}}-\mathbf{n}_{0\mathrm{IV}}) \tag{29a}$$

$$\mathbf{G}_{,2}(\mathbf{0},\theta^3) = \frac{1}{2}(\mathbf{R}_{\mathrm{III}}-\mathbf{R}_{\mathrm{I}}) + \frac{\theta^3}{2}(\mathbf{n}_{0\mathrm{III}}-\mathbf{n}_{0\mathrm{I}}) \tag{29b}$$

$$\mathbf{G}_{,3}(\mathbf{0},\theta^3) = \frac{1}{4}\sum_{P=I}^{\mathrm{IV}} \mathbf{n}_{0P} \tag{29c}$$

Introducing the notation $\Delta\mathbf{R}_{\mathrm{I}} = \frac{1}{2}(\mathbf{R}_{\mathrm{III}}-\mathbf{R}_{\mathrm{I}})$, $\Delta\mathbf{R}_{\mathrm{II}} = \frac{1}{2}(\mathbf{R}_{\mathrm{II}}-\mathbf{R}_{\mathrm{IV}})$, $\Delta\mathbf{n}_{0\mathrm{I}} = \frac{1}{2}(\mathbf{n}_{0\mathrm{III}}-\mathbf{n}_{0\mathrm{I}})$ and $\Delta\mathbf{n}_{0\mathrm{II}} = \frac{1}{2}(\mathbf{n}_{0\mathrm{II}}-\mathbf{n}_{0\mathrm{IV}})$, Equation (28) can be written as

$$\int_\alpha^{h+\alpha} \Bigg[\theta^3 \underbrace{(\Delta\mathbf{R}_{\mathrm{II}}\times\Delta\mathbf{R}_{\mathrm{I}})\cdot\mathbf{G}_{,3}}_{\lambda_1} + (\theta^3)^2 \underbrace{(\Delta\mathbf{n}_{0\mathrm{II}}\times\Delta\mathbf{R}_{\mathrm{I}} + \Delta\mathbf{R}_{\mathrm{II}}\times\Delta\mathbf{n}_{0\mathrm{I}})\cdot\mathbf{G}_{,3}}_{\lambda_2}$$

$$+ (\theta^3)^3 \underbrace{(\Delta\mathbf{n}_{0\mathrm{II}}\times\Delta\mathbf{n}_{0\mathrm{I}})\cdot\mathbf{G}_{,3}}_{\lambda_3} \Bigg]\,\mathrm{d}\theta^3 = 0 \tag{30}$$

which results in a cubic (the quartic terms cancel) equation

$$\lambda_3\alpha^3 + \left(\lambda_2 + \frac{3}{2}\lambda_3 h\right)\alpha^2 + (\lambda_1 + \lambda_2 h + \lambda_3 h^2)\alpha + \frac{\lambda_1 h}{2} + \frac{\lambda_2 h^2}{3} + \frac{\lambda_3 h^3}{4} = 0 \tag{31}$$

In the authors' knowledge, it is the first time the correct procedure for determining the domain of integration of θ^3 is carried out in the finite element context. We use Cardano's formula to determine the zeros, and, according to $\alpha \in [-h, 0]$, select the correct zero.

Introducing another thickness curvilinear co-ordinate $\theta^{3*} \in [-1, 1]$, we can write

$$\theta^3 = \frac{1-\theta^{3*}}{2}\,\alpha + \frac{1+\theta^{3*}}{2}(h+\alpha) \tag{32}$$

and the internal virtual work δW_{I} for a given element e, takes the form (according to the continuum counterpart in Equations (5) and (6))

$$\delta W_{\mathrm{I}}^{e} = \int_{[-1,1]^3} s^{\alpha\beta}\mathbf{x}_{,\beta}\cdot\delta\mathbf{x}_{,\alpha}\,\frac{h}{2}\,\sqrt{G}\,\mathrm{d}\theta^1\,\mathrm{d}\theta^2\,\mathrm{d}\theta^{3*} \tag{33}$$

where the integration domain is now the tri-unit cube $[-1, 1]^3$.

4. NUMERICAL RESULTS

4.1. Remarks on the numerical tests

We perform a series of tests, both in the linear and geometrically non-linear range, to assess the accuracy and versatility of the proposed shell model and finite element. We name the previously described element as QBM to indicate that it is a quadrilateral (Q) with bending (B) and membrane (M) energy. For conciseness, we present most results in graphical form and denote the corresponding reference by the name of the *first* author, to facilitate the readability of the results. All examples were carried out in the software Simplas, created by the first author of this paper.

4.2. Linear beam problems

We test four well-known benchmarks for beam bending (see Figure 4): a cantilever beam with regular mesh, the same beam with mesh distortion, a circular curved beam and a twisted beam. It is important to note that, with the exception of the twisted beam, the loads correspond to unitary analytical values of the transverse displacement at the monitored points. One purpose of these tests is to detect any fundamental deficiency such as spurious mechanisms that occur with coarse meshes. Another interesting result that can be obtained is the effect of using the correct thickness integration instead of the approximate one (typically employed in the degenerated elements).

Starting with the cantilever beam with regular mesh (Beam I in Figure 4) we inspect the convergence of QBM element with mesh refinement, as illustrated in Table I. The monitored value is the transverse displacement under load. Some very slight deviation from the analytical result is obtained.

The same exercise is repeated for the 2 element mesh, Beam II, introducing a distortion parameter a as in Figure 4. For this case, we monitor the normalized tip deflections of points P and Q in Table II. For comparison, we run the same example with the 18 degrees-of-freedom element of Reference [8], whose accuracy is usually very high for *undistorted* meshes. The effect of this distortion is striking for the performance of 3D EAS elements (other EAS elements

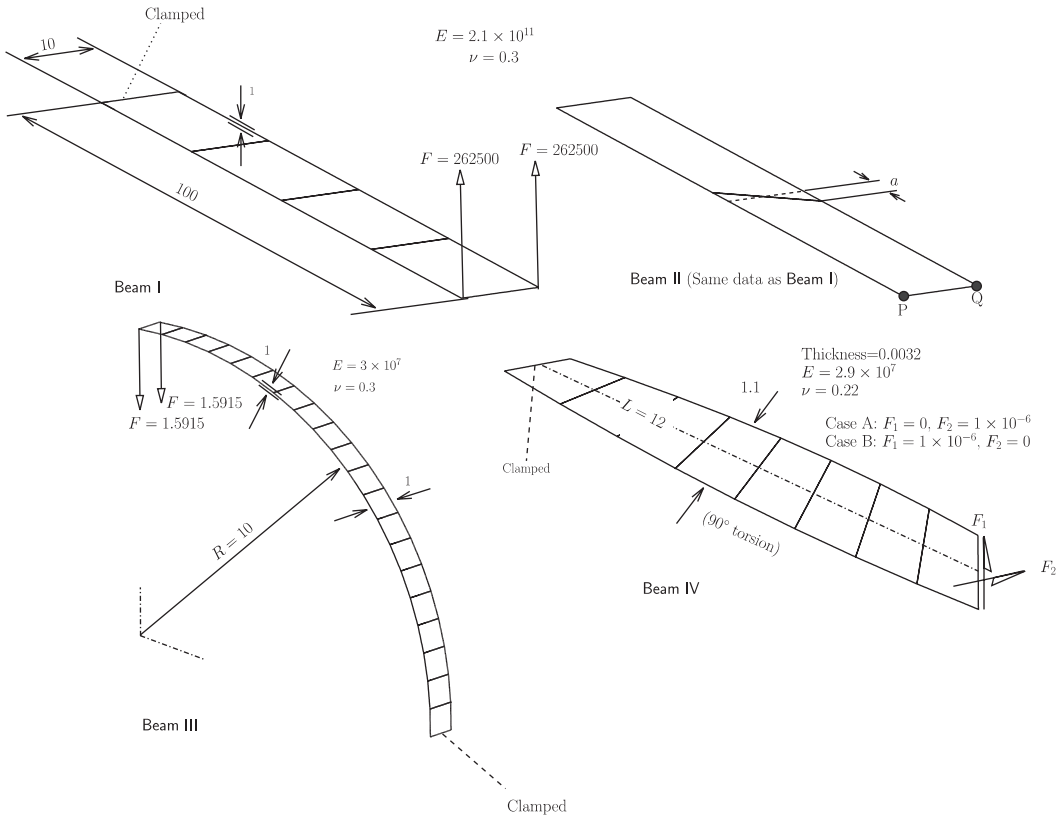

Figure 4. Linear elastic analysis of beams: geometry, boundary conditions and material properties.

Table I. Beam I: convergence with mesh refinement.

Number of elements	QBM, normalized displacement
2	0.9520
3	0.9853
4	0.9958
6	1.001
8	1.002
10	1.002

show similar or worse performance under distortion, see Reference [8]), and only mild for the present QBM element. It is interesting to note that, despite the obvious degradation in the results with distortion, the symmetry of the displacement values is reasonably preserved for the QBM element.

For the circular arch (Beam III in Figure 4), we show the convergence with mesh refinement, and compare the normalized results with the ones in Reference [46] for the hexahedron

Table II. Beam II: effect of mesh distortion (introduced through parameter a) in the normalized transverse displacement, comparison with element HIS described in Reference [8].

a	QBM, point P	QBM, point Q	HIS, point P	HIS, point Q
0	0.9520	0.9520	0.9376	0.9376
5	0.9042	0.9043	0.0020	0.0033
10	0.7839	0.7832	0.0002	0.0027

Table III. Beam III: normalized results as a function of mesh topology.

Mesh topology	QBM	HUHEXIN-4 [46]	HIS [8]
3×1	0.932966	*	*
4×1	0.963842	*	*
5×1	0.977530	0.787	0.8418
6×1	0.984851	*	*
8×1	0.991217	*	*
10×1	0.993763	*	*
20×1	0.996310	*	*
40×1	0.996628	*	*
$10 \times 2 \times 2^{\dagger}$	0.9893	0.998	0.9955
$20 \times 4 \times 4^{\ddagger}$	0.9918	1.023	1.012

*Not available.
$^{\dagger}10 \times 2 \times 1$ for QBM.
$^{\ddagger}20 \times 4 \times 1$ for QBM.

HUHEXIN-4 and with the values of Reference [8] for the element HIS. Table III summarizes the results, with the first column indicating the element arrangement along the circumferential direction, the width and the thickness (the latter is used in the aforementioned 3D elements), respectively.

This example provides an opportunity to examine the distribution of α along the beam. Two situations can be envisaged: piecewise constant undeformed directors and 'continuous' directors obtained from averaging neighbourhood elements. As all elements contain co-planar nodes, the distribution of α is uniform and equal to -0.5 for piecewise constant directors, and varies from element to element if average undeformed directors are employed. For this situation, Figure 5 shows the results.

For the pre-twisted beam (Beam IV in Figure 4) we present results for the two depicted load cases, A and B, whose reference tip displacement in the direction of the load is 5.256×10^{-3} and 1.294×10^{-3}, respectively (c.f. Reference [9]). This test was proposed by MacNeal and Harder [47] and modified, through a reduction in thickness, by Belytschko and Wong [9]. We follow the latter reference in our benchmark. The normalized tip displacements are shown in Table IV, where a comparison with the 4 node uniformly reduced integrated element (URI) documented in Reference [9] and with the hybrid stress element $H8$ by Sze *et al.* [48] is observable. Note that a different version of this test was proposed by Simo *et al.* [7]. The

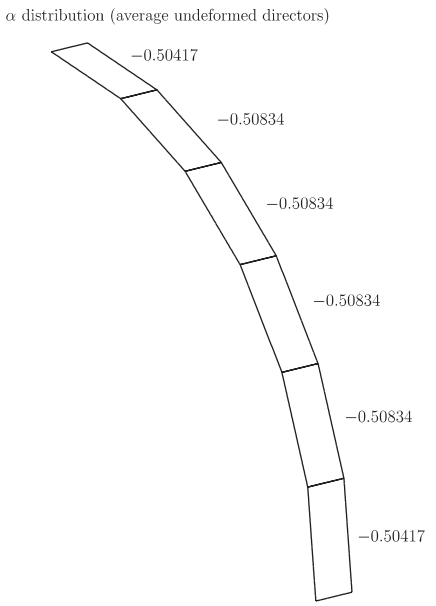

Figure 5. Distribution of α for the circular arch with 6 elements ($\alpha = -0.5$ corresponds to the traditional thickness quadrature).

Table IV. Beam IV: normalized results as a function of mesh topology. Case A corresponds to in-plane bending and case B to out-of-plane bending.

Mesh	QBM, A	QBM, B	URI, A[9]	URI, B[9]	H8, A[48]	H8, B[48]
2×1	0.9793	0.5299	*	*	*	*
4×1	1.0120	0.8949	*	*	*	*
6×1	1.0180	0.9650	*	*	1.023	0.979
8×1	1.0190	0.9880	*	*	*	*
10×1	1.0180	0.9985	*	*	*	*
10×2	0.9922	0.9784	*	*	*	*
12×2	0.9951	0.9877	1.007	0.984	*	*
20×2	0.9942	0.9984	*	*	*	*

*Not available.

results are remarkable, and for case A, with one element, the tip displacement error is only 11.8%. It can be seen in Table IV that the in-plane bending (case B) accuracy of the element is not as good as its out-of-plane bending (case A), because no special treatment is employed for the former. This fact limits the in-plane performance to the one observed with standard iso-parametric quadrilaterals.

4.3. Linear plate bending problems

We test 3 plate problems. Figure 6 shows the geometry, boundary conditions and relevant elastic material properties. Plates I and III are submitted to point loads. Plate I is a clamped

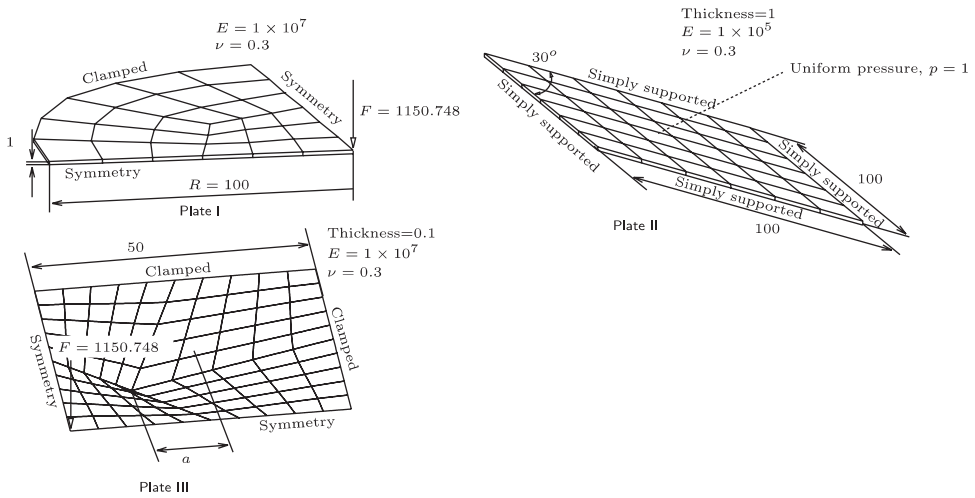

Figure 6. Linear elastic bending of plates.

circular plate, plate II is a (simply supported) 30° skew plate under uniform pressure. To verify (and compare) mesh sensitivity, we use plate III with the 10×10 element mesh shown. This mesh is formed by dividing the quarter plate into four mesh domains, where the common point of the domains is displaced by a towards the load point. The results are normalized with the Kirchhoff plate theory (see Reference [49]) for plates I and III.

The solution of the circular plate problem is interesting, since the clamped boundary is represented by straight-edged elements. The best results obtained with reduced integration hexahedral elements (see References [8, 46, 50]) are used for comparison. In Reference [46], the best results were obtained with the NUHEXIN-4 element, and these are presented here for comparison. Figure 7 summarizes the results.

For the skew plate, the target displacement at the centre of the plate with value 4.64 consistent units is to be expected for shear-deformable models, as stated in Reference [51], whereas the thin plate solution is Morley's 4.455 [52]. In our test, a comparison with References [8, 51, 53, 54] is carried out. The values of Reference [51] are the ones of shell element EAS7-ANS. Figure 8 shows the convergence of the results. Because two distinct solutions are usually presented for the central displacement, according to the model in use, we do not normalize these results (see also Reference [7] for further discussion). Finally, to study the plate mesh distortion effect, the results for plate III are shown in Table V.

4.4. Linear shell problems

The linear shell problems considered are depicted in Figure 9, where a circle indicates the position of the monitored quantity. Shell I consists of pinched cylinder with rigid end diaphragms and has been analysed, among others, in References [7, 8, 48, 55–58], whose results are reproduced here for comparison. The values corresponding to the 4 node selectively integrated quadrilateral (SRI) are taken from Reference [9]. A value of 1.82488×10^{-5} (c.f. Reference [59]) consistent units is adopted as a reference for the pinched displacement under load.

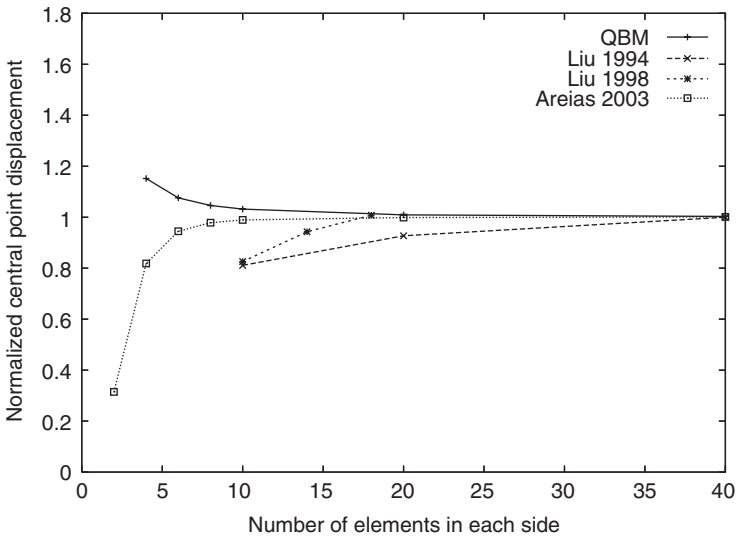

Figure 7. Circular plate (Plate I): comparison with References [8, 46, 50].

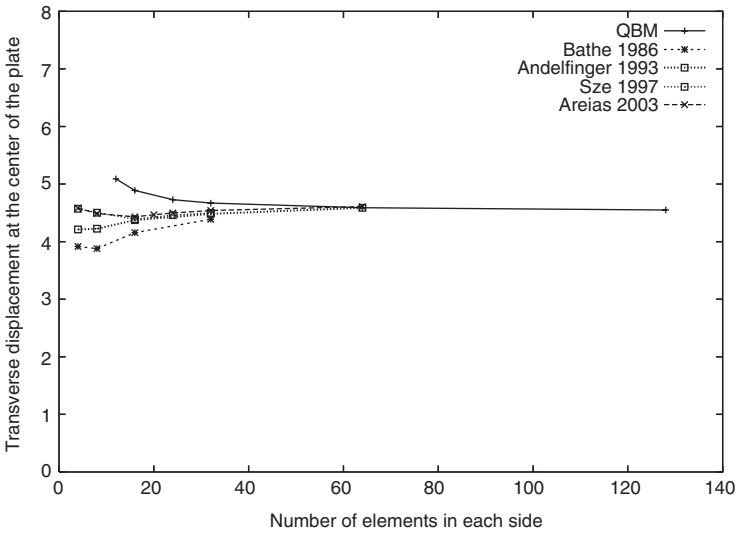

Figure 8. Skew plate (Plate II): comparison with References [8, 46, 50].

Shell II is a closed hemisphere under two point loads, whose reference radial displacement is 0.0924 (c.f. Reference [50]). Results from References [7, 8, 55, 60, 61] are used for comparison, along with the 4 node SRI. Shell III is a variant of shell II, with a 18-degree opening. A reference value of 0.094 is adopted (see, e.g. Reference [59]) for the radial displacement under the loads and the results used for comparison are those of References [7, 8, 57, 59, 62, 63]. The

Table V. Plate III: normalized results as a function of the distortion parameter a.

a	QBM
0	1.04100
2.5	1.03900
5	1.03800
7.5	1.03700
10	1.03600
15	1.03500

values of Reference [7] were re-normalized to give a correct comparison, as Simo *et al*. used 0.093 as a reference value.

Shell IV is a 'partly clamped hyperbolic paraboloid' [64] and was proposed in Reference [64] as a bending-dominated test for shell elements. According to this reference, two of the recommended values of thickness are tested: 0.01 and $0.001\,\mathrm{m}$. For the first situation, the total strain energy reference is $E_n = 1.679 \times 10^{-3}\,\mathrm{N\,m}$, and for the second situation, the reference value is $E_n = 1.1013 \times 10^{-2}\,\mathrm{N\,m}$. These values were suggested, based on numerical experiments, in Reference [64].

Shell V is the Scordelis-Lo roof [47] and consists of a shallow cylindrical shell supported by rigid diaphragms and subjected to its weight. The monitored node has a reference vertical displacement of 0.3086 consistent units [47]. Results from References [7, 8, 54] are employed in the comparison. It is important to note that the values presented here from Reference [7] was re-normalized, as other reference values were proposed (the value 0.3008 is proposed in Reference [51], and 0.3024 is employed in Reference [7]) for the transverse displacement at the mid-side.

The results for shell I are shown in Figure 10. We note that, despite the somehow soft behaviour for moderately coarse meshes (only 4, 5, 7, 8, 30 and 32 elements per side are shown for QBM), the results are very good overall.

For the closed and open hemispheres (shells II and III), the results are presented in Figures 11 and 12, respectively. The results are remarkable, as no enhancement exists in the present element, in contrast with Reference [8].

For shell IV, we note that, despite inadequate accuracy for coarse meshes (see Figure 13), the energy error is lower than the one observed in Reference [64] (the MITC4 element) for sufficiently refined meshes. A similar observation was made in Reference [8] concerning the HIS 3D element. With respect to the Scordelis-Lo roof (shell V), we note that the QBM element's performance is comparable to the one shown by the previous HIS 3D element (Figure 14).

4.5. Pure bending of a beam

This classical geometrically non-linear solid mechanics problem (described in Reference [65]) consists of an elastic cantilever beam subject to a bending moment on one end and clamped on the opposite end. The moment is gradually increased until the beam middle surface forms a perfect cylinder. This problem has been solved numerically in several papers. Recently, in References [66, 67] a simulation of this test was carried out in the context of validating procedures for finite rotation of shell elements and in Reference [8] it was used to test a

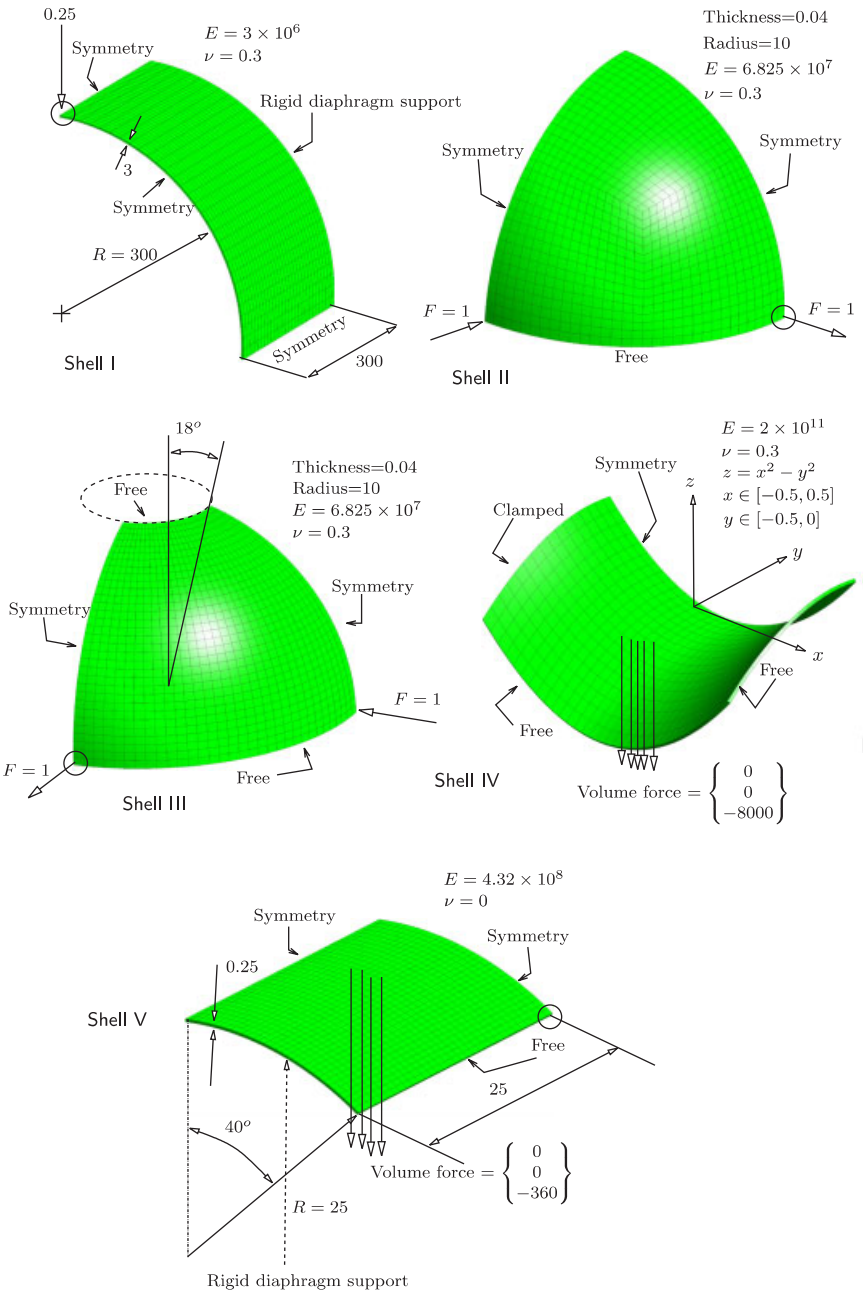

Figure 9. Geometry, boundary conditions and material properties for 5 linear shells.

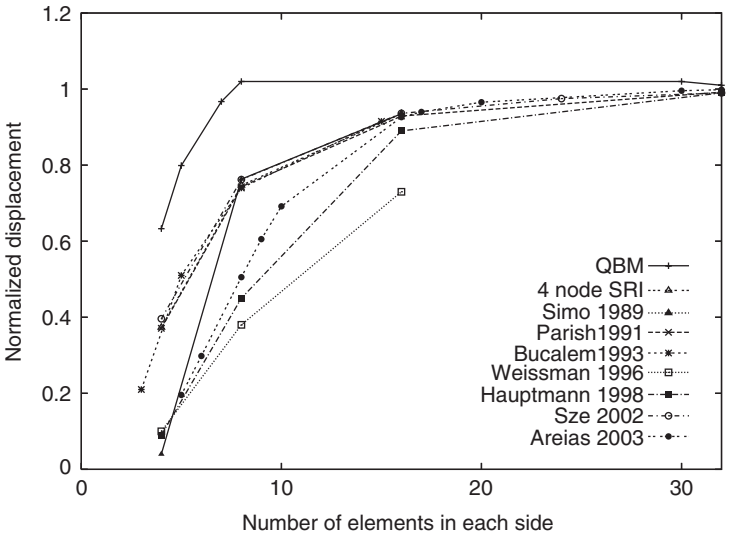

Figure 10. Shell I: pinched cylinder with rigid diaphragm. Comparison of the normalized load-point displacement.

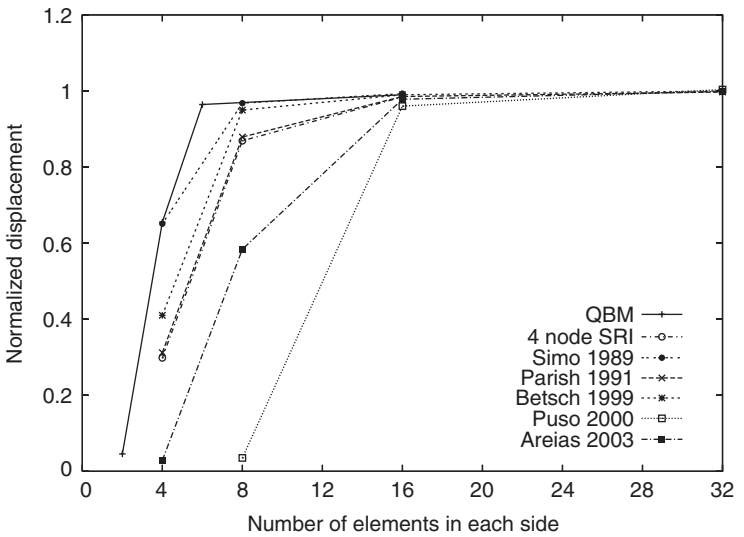

Figure 11. Shell II: closed hemisphere. Convergence of the normalized displacement.

hexahedral element. The geometry and boundary conditions described in References [66–68] are here reproduced. For the end moment, M, the following formula is employed (see also Reference [68]):

$$M = \frac{2EI\pi n}{L} \tag{34}$$

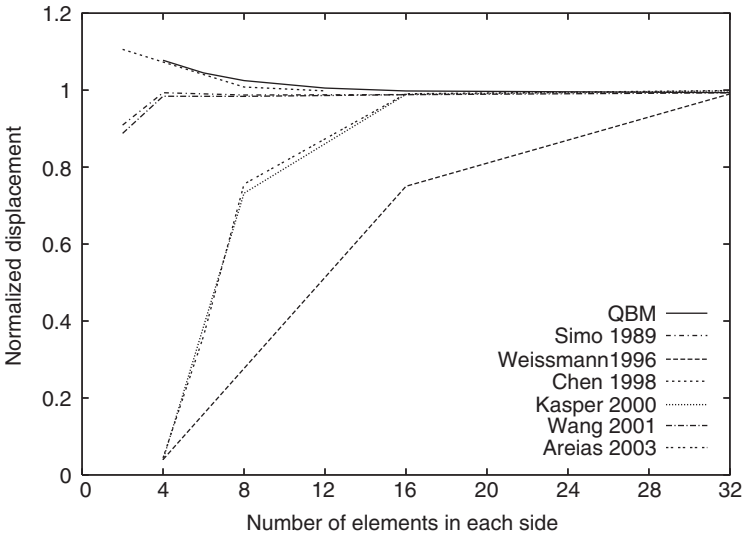

Figure 12. Shell III: open hemisphere. Convergence of normalized displacement.

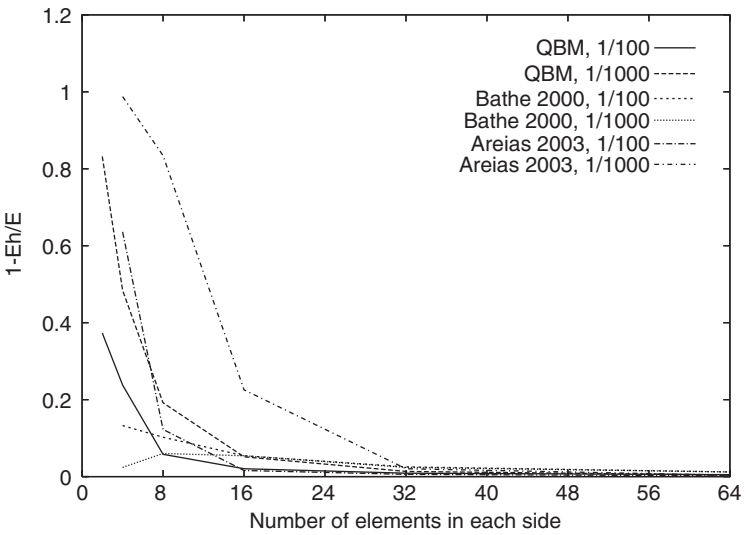

Figure 13. Shell IV: hyperbolic paraboloid. Convergence of strain energy error for two values of thickness.

where E represents the Young's modulus, I represents the second order moment of the cross-section relative to the bending moment direction and L represents the beam length. The integer n represents the number of complete turns of the beam. For this problem the Poisson coefficient is $v = 0$ and the Young's modulus is $E = 1.2 \times 10^7$.

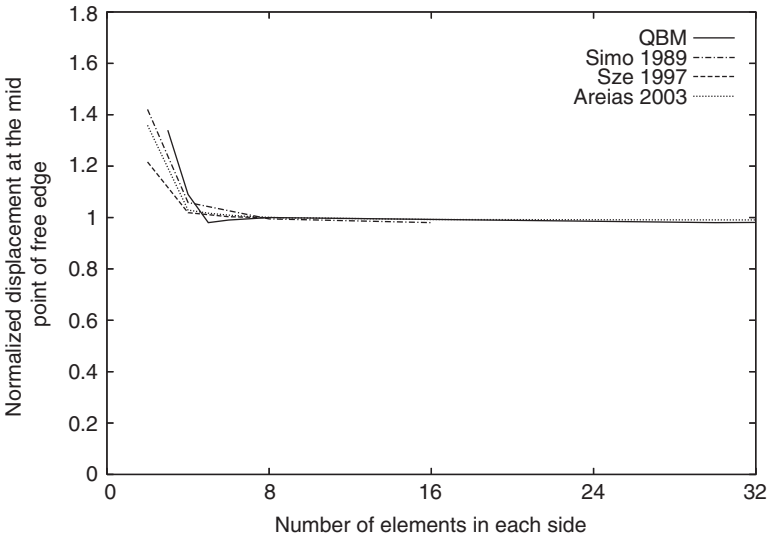

Figure 14. Shell V: Scordelis-Lo roof. Convergence of normalized mid-side displacement.

Figure 15 presents the 15 element mesh and the boundary conditions in the undeformed case for $\theta = 0$, and also several steps during the deformation. In Reference [68] a 20×1 element mesh was used and in Reference [66] the same problem was analysed with a 25×2 shell element mesh. For comparison purposes, we use the values of Reference [68], as depicted in Figure 16.

4.6. Hinged cylindrical shell under a central point load

This test has been considered by Sabir and Lock [69] and later by Ramm [70], and it is a popular test (a non-exhaustive list of other references where this test has been studied includes References [67, 71–76]). The test is useful to verify both the non-linear finite element formulation and the path following algorithms.

It consists of a pinched shallow cylinder with hinged longitudinal edges and free curved edges, as depicted in Figure 17. Due to symmetry, only one quarter of the model is actually meshed. A thickness of $6.35\mathrm{mm}$ is known to induce both snap-through and snap-back behaviour, as detailed in Reference [71]. In this work, a standard spherical arc-length procedure is adopted which is analogous to the one described in Reference [70]. In terms of results, we compare ours with Reference [70] where a 2×2 mesh of bi-cubic 16-noded elements was employed. The vertical displacement of points A and B identified in Figure 17 is monitored. We use a 6×6 element mesh as depicted in Figure 17. The material is considered elastic with a Young's modulus of $E = 3.103 \times 10^3\ \mathrm{N/mm^2}$ and a Poisson coefficient $\nu = 0.3$.

The load–deflection curves for points A and B are shown in Figure 18 with excellent agreement with the high order 16 node element of Ramm [70].

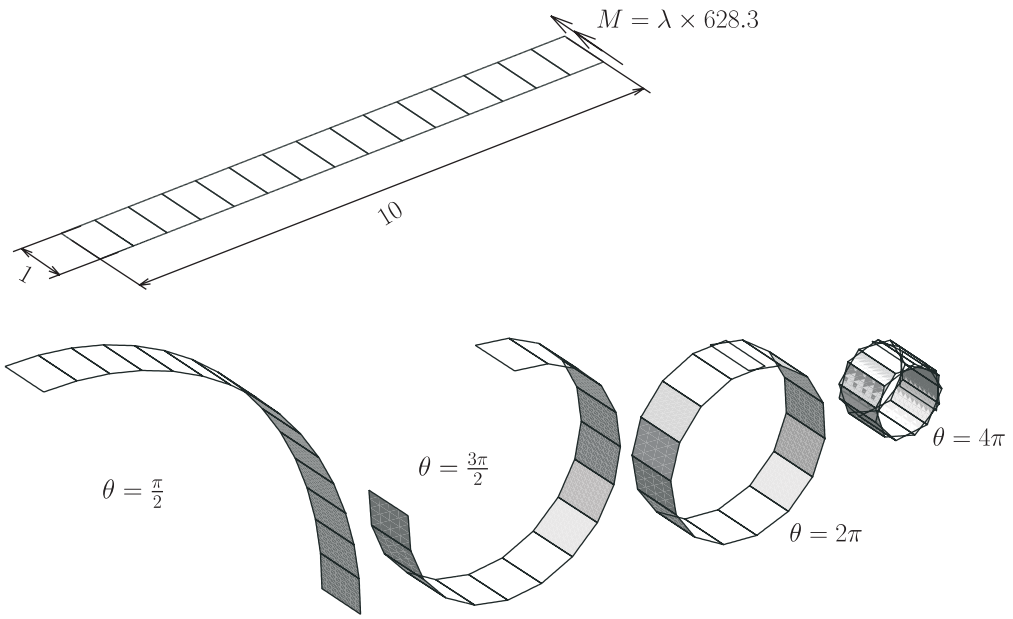

Figure 15. Pure bending of a beam: relevant data and deformed meshes for $\theta = \pi$, $\theta = 3\pi/2$, $\theta = 2\pi$ and $\theta = 4\pi$.

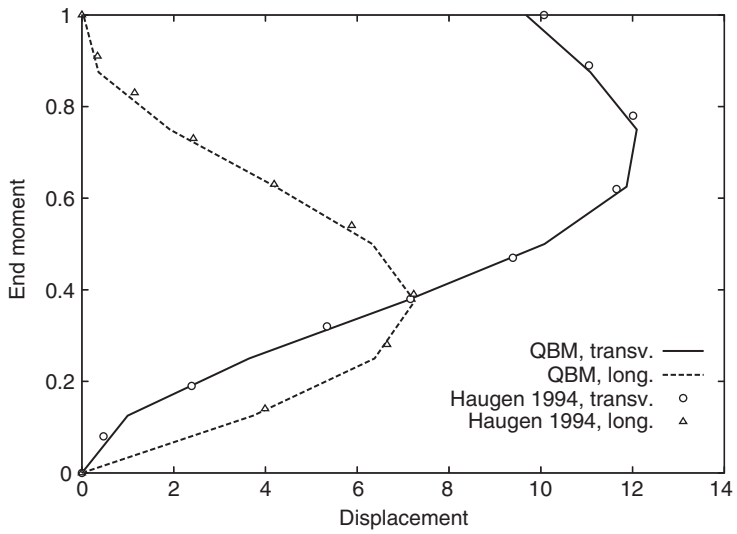

Figure 16. Pure bending of a beam: comparison of longitudinal (long.) and transverse (transv.) displacements with the ones of Reference [68].

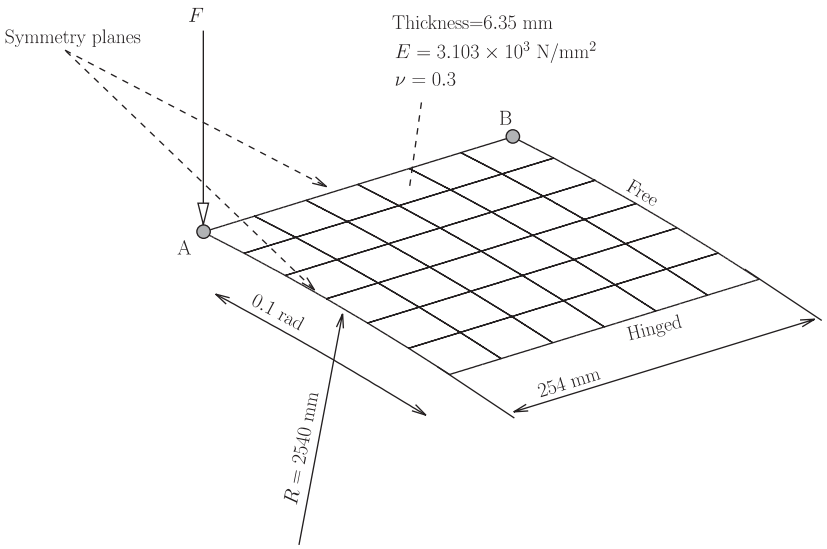

Figure 17. Hinged cylindrical shell: geometry, mesh and boundary conditions for one quarter of the shell.

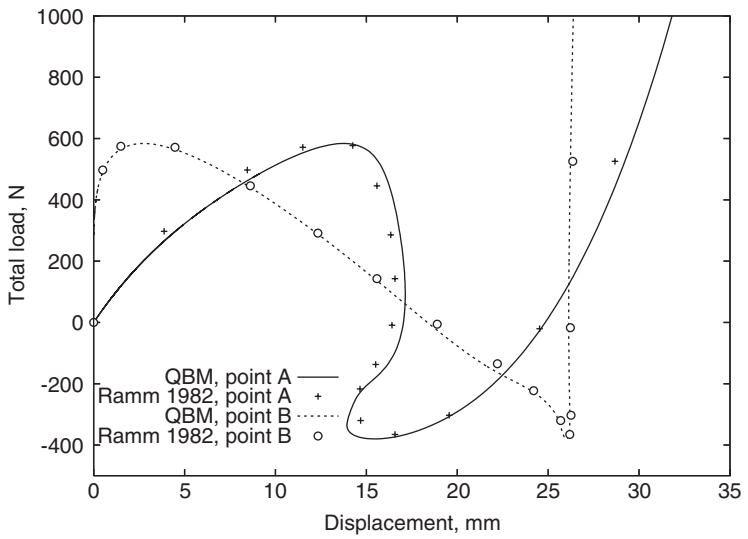

Figure 18. Hinged cylindrical shell: load–deflection curve for points A and B, comparison with Reference [70].

4.7. Clamped frame problem

This problem was introduced by Argyris *et al.* [3] and further investigated by Nour-Omid and Rankin [77] in the context of validating co-rotational formulations based on element frames. Our purpose here is to inspect, using the same 64 element mesh tested in the latter reference, the post-buckling behaviour of the QBM element.

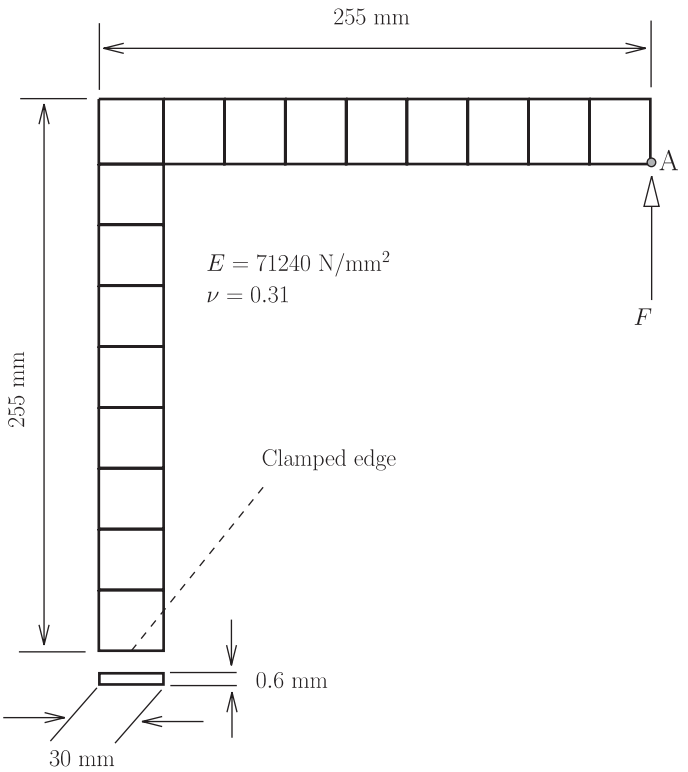

Figure 19. Relevant data for the clamped right-angle frame problem.

The relevant data corresponding to this problem is depicted in Figure 19. The deformed mesh for a load of $F = 18\,\mathrm{N}$ is depicted in Figure 20, along with the undeformed counterpart. The load–deflection curve is compared with the results of Reference [77] in Figure 21.

4.8. Pinching of a short clamped cylinder

This test was carried out in References [44, 78, 79] in the context of representing finite rotations in shell elements. A cylindrical shell is clamped at one end and it is subject to two diametrically opposite forces in the other end. For further details, consult References [44, 76, 79, 80].

Our objective in inspecting this problem is that it was discovered by Crisfield and Peng [79] that the Morley triangle showed severe 'artificial' instabilities for coarse meshes. As the Morley triangle can be viewed as a simplified counterpart of the present QBM element, it is interesting to inspect the existence of such instabilities.

The dimensions, material properties and boundary conditions for one-fourth of the geometry are depicted in Figure 22. A regular 16×16 element mesh is employed, in agreement with Reference [44]. It is noticeable that this is a known test to verify the behaviour of the element under inextensional deformations [80].

Four different load steps are represented in Figure 23. The comparison of the results obtained with element QBM, the *variation* of the MITC4 element proposed in References [44, 81] and the

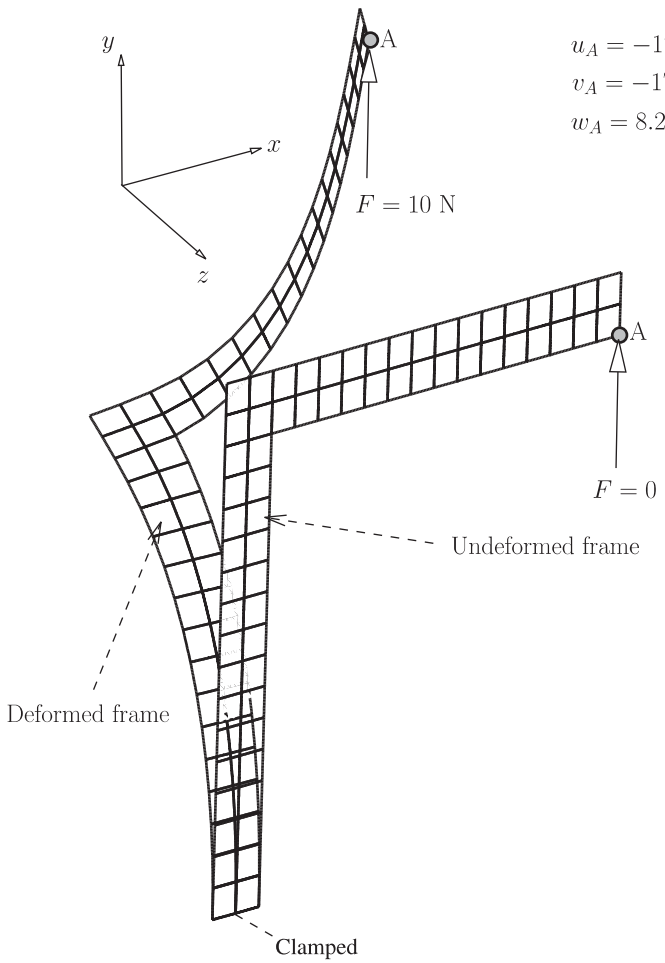

Figure 20. Clamped frame problem: undeformed mesh and deformed mesh for a load of $F = 10\,\mathrm{N}$.

MTRIC shell element [76] is shown in Figure 24. No instabilities such as the ones described in Reference [79] were noted. Two additional conclusions can be readily extracted from Figure 24: there is a close agreement with the results of the above references and much higher values of load can be imposed, without failure of convergence.

4.9. Thin plate ring

This problem was first considered by Basar and Ding [82] to test formulations for finite shell rotations. Several other authors have studied this problem (e.g. References [83–86]). The test consists in the pulling of a thin circular ring containing a radial cut. The pulling is carried out by a distributed load in a fixed direction, applied on a edge. The opposite edge is clamped.

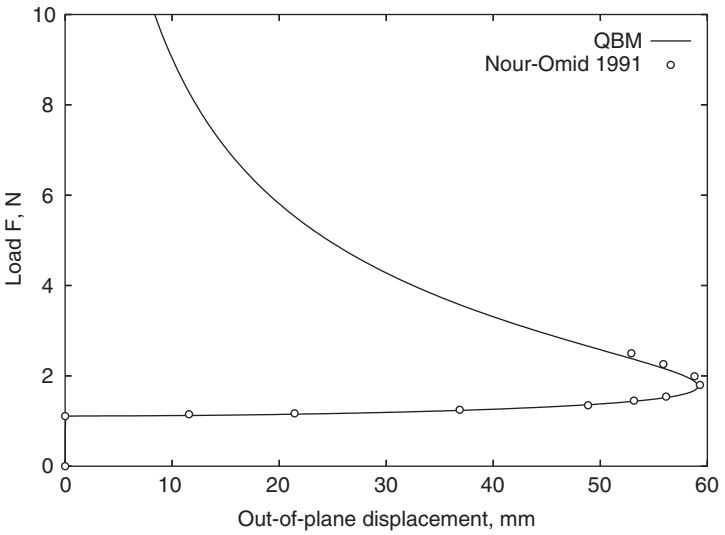

Figure 21. Clamped frame problem: load–deflection curve, comparison with Reference [77].

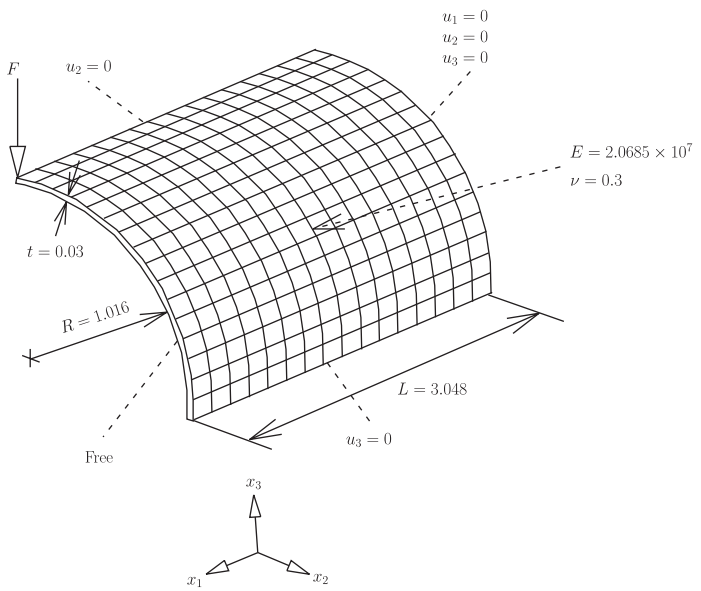

Figure 22. Clamped cylinder: geometry, mesh, boundary conditions and material properties, in agreement with References [44, 76].

The ring is considered elastic with Young's modulus $E = 2.1 \times 10^{10}$ and Poisson coefficient of $v = 0$. The geometry, mesh, and boundary conditions are represented in Figure 25, along with a highly deformed configuration. It is noted that, despite the localized mesh distortion, as can

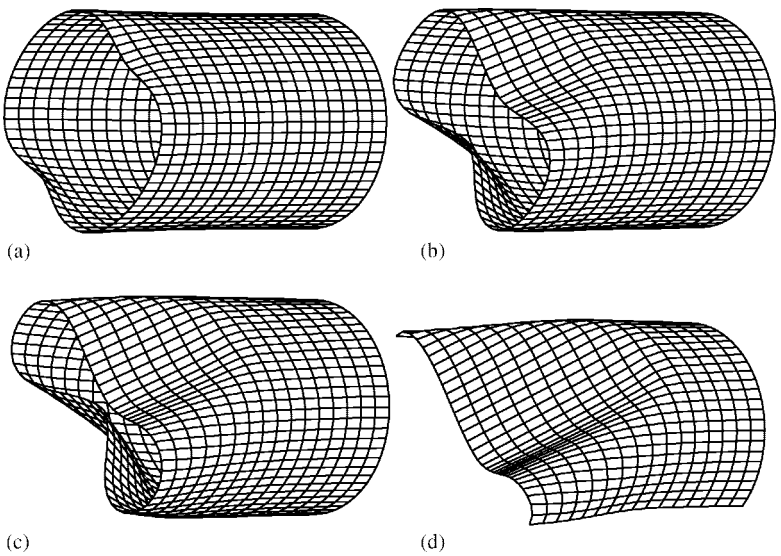

Figure 23. Clamped cylinder: several deformed meshes for increasingly higher load values.

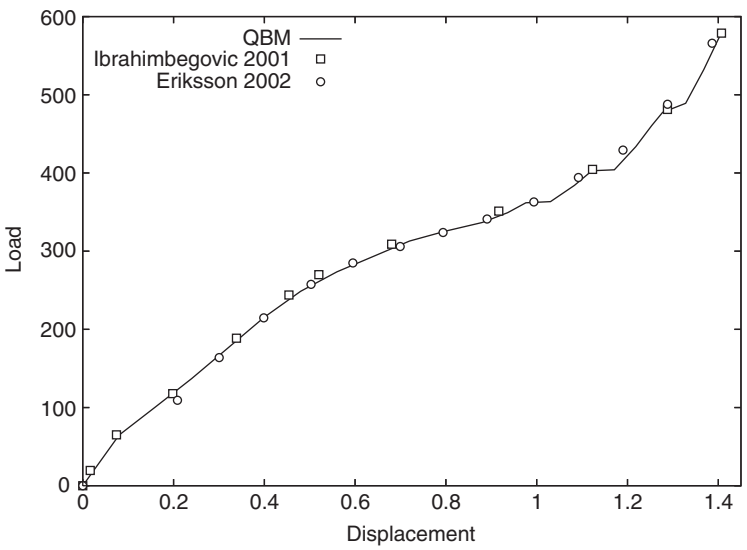

Figure 24. Clamped cylinder: load–displacement relation. Comparison with the results obtained in References [44, 76].

be observed, there are few consequences in terms of the results. The mesh contains $6 \times 30 \times 1$ elements as in Reference [86], where 3 types of shell elements (hybrid strain, hybrid stress and enhanced strain) were tested with similar results for this mesh. For comparison purposes, the results of Reference [86] are adopted, as noted in Figure 26.

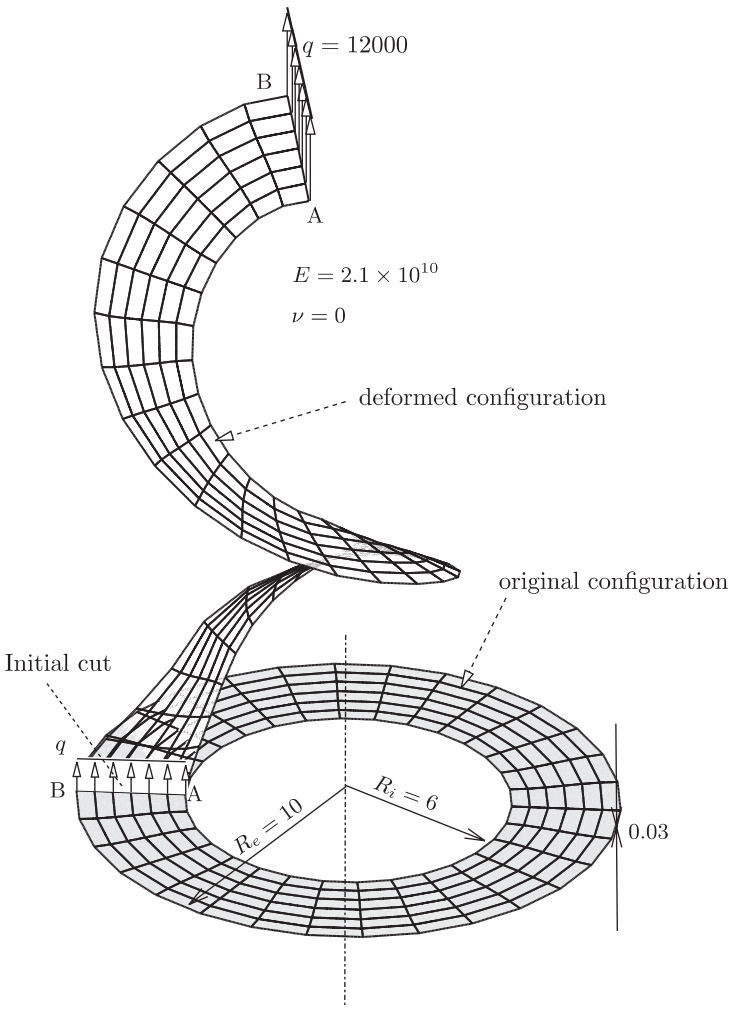

Figure 25. Thin plate ring: geometry, boundary conditions and deformed mesh for a load magnitude of $q = 12\,000$ consistent units (note the distorted mesh due to deformation). The shell on the clockwise side of line AB is fixed, on the other side is free and loaded vertically (load q).

4.10. Pullout of an open cylinder

This example has been described and studied by various other authors (e.g. References [32, 72, 84, 86–88]) and constitutes a difficult test for finite element formulations, combining bending and membrane effects. It consists of a cylinder shell with open ends which is pulled at two diametrically opposite points through the application of point loads. The geometry, mesh and boundary conditions for one-eighth of the model are presented in Figure 27. Point A in Figure 27 is monitored in terms of absolute radial displacement. The material is considered elastic, with Young's modulus $E = 10.5 \times 10^6$ consistent units and Poisson coefficient

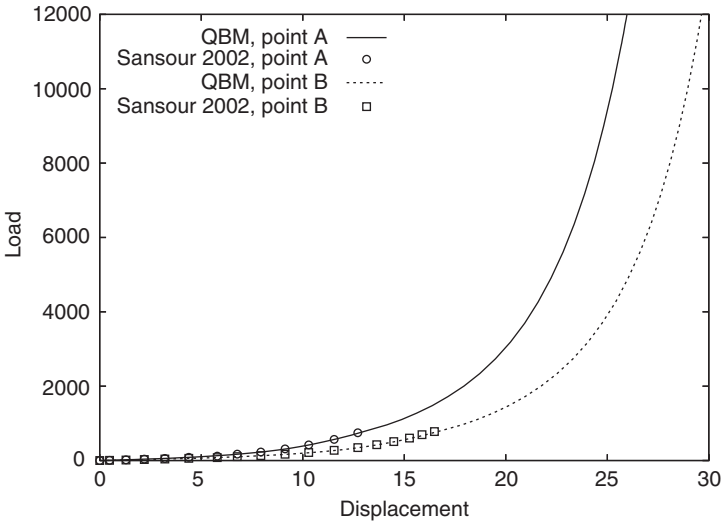

Figure 26. Thin plate ring: load–displacement results for points A and B.

$v = 0.3125$, in agreement with the above references. A mesh containing 16 elements along the circumferential direction and 8 elements along the longitudinal direction is employed. A similar mesh has been used in Reference [87]. The absolute radial displacement for point A is compared with the values obtained in References [32, 87]. Figure 28 shows this comparison. It is noticeable that triangles were employed in Reference [32] and a coarser mesh. However, this example illustrates the Newton–Raphson characteristics of the QBM element, which can sustain very high levels of distortion without performance degradation.

4.11. Open hemisphere loaded by alternating forces

This example is a non-linear counterpart of the linear elastic *open* hemisphere example illustrated in Figure 9. The shell undergoes large displacements but strains and rotations are relatively small (c.f. Reference [66]). This test is widely studied, see References [58, 63, 66, 72, 84–87, 89–91]. Figure 29 shows half of a deformed hemisphere with 24×24 elements. Nodes A and B, identified in the figure, are monitored in terms of absolute radial displacement. The material is considered elastic with a Young's modulus $E = 6.825 \times 10^7$ and a Poisson coefficient $v = 0.3$. The mean radius is 10 and the thickness 0.04. Only one quarter of the model is actually meshed with two mesh densities: 16×16 elements and 24×24 elements. Most authors use a 16×16 mesh, but Reference [85] shows results for a 24×24 mesh. Reference [58] uses a even finer 32×32 mesh.

A comparison, in terms of point load/radial displacement, between the present formulation and the ones of References [66, 85, 86] is presented in Figure 30. Very good agreement for the 16×16 element mesh is obtained between the present formulation and the above references using the same mesh. It is clear that a much higher level of load can be achieved by the QBM formulation, without loss of convergence.

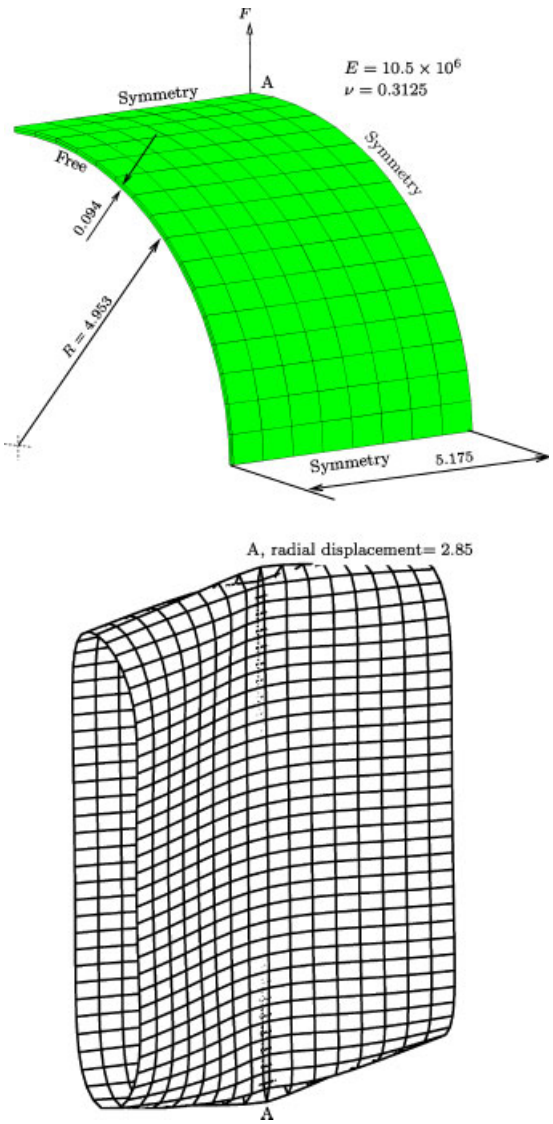

Figure 27. Pulled cylinder with free edges: geometry, mesh and boundary conditions for one-eighth of the model, and deformed mesh for a radial displacement of 2.85 consistent units.

5. CONCLUSIONS

We have described a non-conventional formulation for shell analysis based on a classical shell theory with Kirchhoff–Love constraints. These were concisely written as $C_{i3} = \delta_{i3}$ and were imposed by appropriate transformations to define the director field. We combined a continuum (i.e. non-integrated) constitutive law with classical shell kinematics. From the application

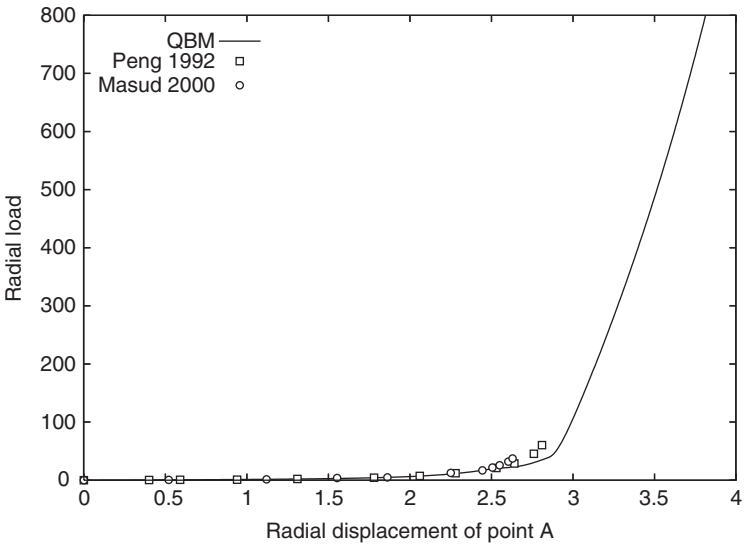

Figure 28. Pulled cylinder with free edges: comparison of load–displacement curves with References [32, 87].

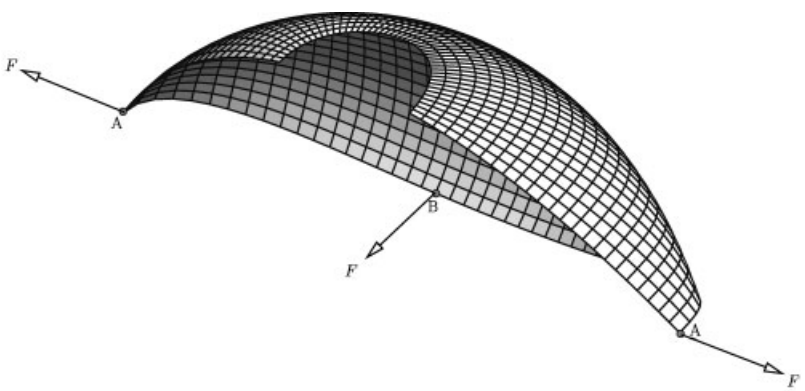

Figure 29. A deformed configuration of the (half) open hemisphere loaded by alternating point forces. The picture corresponds to $F = 104$ consistent units.

viewpoint this constitutes a distinct advantage, as available *continuum* constitutive models can be employed without modification and the specific shell kinematics remove the need of accounting for the transverse shear energy (which, for large strain elasto-plasticity, is frequently assumed to be of elastic origin only, see Reference [31]).

The finite element implementation made is based on a four node quadrilateral with 4 mid-side rotations and 4 nodes, each with 3 displacement degrees-of-freedom. Each of the constraints $C_{13} = 0$ and $C_{23} = 0$ is enforced at two mid-side points in opposing sides and $C_{33} = 1$ is enforced at all four mid-sides by means of transformation of the directors. A novel method was

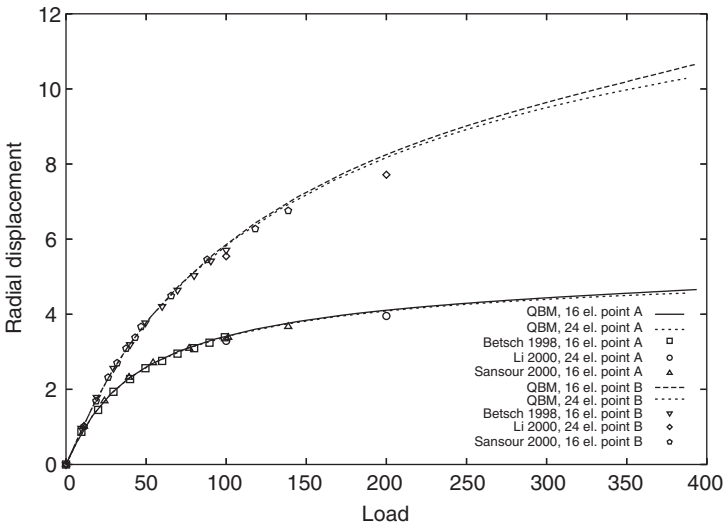

Figure 30. Open hemisphere: comparison of load–displacement curves with References [66, 85, 86].

developed for the mid-side director that conveniently enforces the Kirchhoff–Love constraint and is applicable to arbitrarily large rotations. The element can be classified as a discrete Kirchhoff type of element. We developed symmetric shape functions for the director field and based the model on classical Naghdi shell theory [20] (neglecting the transverse shear energy terms). Five quadrature points were employed for each element, along two lines bisecting the parent domain, circumventing the difficulties previously associated with warped elements. We also proposed a (simplified) calculation for identifying the mid-surface position in each element. The performance of the element in the tests in both linear and non-linear regimes was very good, when compared with other high performance elements available in the literature, some of them making use of internal degrees-of-freedom (e.g. Reference [8]). In particular, mesh distortion sensitivity was extremely low. It is worth noting that the implementation did not make use of any significant assumptions besides the ones inherited from the proposed model. Extensions of the model and the finite element application are being carried out to deal with ductile fracture.

ACKNOWLEDGEMENTS

The support of the Office of Naval Research is gratefully acknowledged.

REFERENCES

1. Ahmad S, Irons BM, Zienkiewicz OC. Analysis of thick and thin shell structures by curved finite elements. *International Journal for Numerical Methods in Engineering* 1970; **2**:419–451.
2. MacNeal RH. A simple quadrilateral shell element. *Computers and Structures* 1978; **8**:175–183.
3. Argyris JH, Balmer H, Doltsinis JS, Dunne PC, Haase M, Kleiber M, Malejannakis GA, Mlejenek HP, Muller M, Scharpf DW. Finite element method—the natural approach. *Computer Methods in Applied Mechanics and Engineering* 1979; **17/18**:1–106.

4. Hughes TJR, Tezduyar TE. Finite elements based upon Mindlin plate theory with particular reference to the four-node bilinear isoparametric element. *Journal of Applied Mechanics* (ASME) 1981; **48**:587–596.
5. Belytschko T, Stolarski H, Liu WK, Carpenter N, Ong JSJ. Stress projection for membrane and shear locking in shell finite elements. *Computer Methods in Applied Mechanics and Engineering* 1985; **51**:221–258.
6. Simo JC, Fox DD. On a stress resultant geometrically exact shell model. Part I: formulation and optimal parametrization. *Computer Methods in Applied Mechanics and Engineering* 1989; **72**:267–304.
7. Simo JC, Fox DD, Rifai MS. On a stress resultant geometrically exact shell model. Part II: the linear theory; computational aspects. *Computer Methods in Applied Mechanics and Engineering* 1989; **73**:53–92.
8. Areias PMA, César de Sá JMA, Conceição António CA, Fernandes AA. Analysis of 3D problems using a new enhanced strain hexahedral element. *International Journal for Numerical Methods in Engineering* 2003; **58**:1637–1682.
9. Belytschko T, Wong BL. Assumed strain stabilization procedure for the 9-node Lagrange shell element. *International Journal for Numerical Methods in Engineering* 1989; **28**:385–414.
10. Belytschko T, Leviathan I. Physical stabilization of the 4-node shell element with one-point quadrature. *Computer Methods in Applied Mechanics and Engineering* 1994; **113**:321–350.
11. Hughes TJR, Taylor RL, Kanoknukulchai W. A simple and efficient finite element for plate bending. *International Journal for Numerical Methods in Engineering* 1977; **11**:1529–1543.
12. Arnold DN, Brezzi F. Locking-free finite element method for shells. *Mathematics of Computation* 1997; **66**: 1–14.
13. Arnold DN, Brezzi F. The partial selective reduced integration method and applications to shell problems. *Computers and Structures* 1997; **64**:879–880.
14. Wang X-J, Belytschko T. A study of stabilization and projection in the 4-node Mindlin plate element. *International Journal for Numerical Methods in Engineering* 1989; **28**:2223–2238.
15. Park KC, Stanley GM. A curved $\mathscr{C}^0$ shell element based on assumed natural-coordinate strains. *Journal of Applied Mechanics* (ASME) 1986; **53**:278–290.
16. Piltner R, Joseph DS. An accurate low order plate bending element with thickness change and enhanced strains. *Computational Mechanics* 2001; **27**:353–359.
17. Bletzinger K-U, Bischoff M, Ramm E. A unified approach for shear-locking-free triangular and rectangular shell finite elements. *Computers and Structures* 2000; **75**:321–334.
18. Yang HTY, Saigal S, Masud A, Kapania RK. A survey of recent shell finite elements. *International Journal for Numerical Methods in Engineering* 2000; **47**:101–127.
19. Fraeijs de Veubeke B. A conforming finite element for plate bending. *International Journal of Solids and Structures* 1968; **4**:95–108.
20. Naghdi PM. The theory of shells plates. In *Encyclopedia of Physics*, *Mechanics of Solids II*, vol. VIa, Flügge S (ed.). Springer: Berlin, 1972; 425–640 (Trusdell C. Series Editor).
21. Chapelle D, Bathe K-J. The mathematical shell model underlying general shell elements. *International Journal for Numerical Methods in Engineering* 2000; **48**:289–313.
22. Wempner G. Finite elements, finite rotations and small strains of flexible shells. *International Journal of Solids and Structures* 1969; **5**:117–153.
23. Herrmann LR. Finite-element analysis for plates. *Journal of the Engineering Mechanics Division* (ASCE) 1967; **93**(EM-5):13–26.
24. Herrmann LR, Campbell DM. A finite-element analysis for thin shells. *AIAA Journal* 1968; **6**:1842–1847.
25. Batoz JL, Hammadi F, Zheng C, Zhong W. On the linear analysis of plates and shells using a new-16 degrees of freedom flat shell element. *Computers and Structures* 2000; **78**:11–20.
26. Morley LSD. The constant-moment plate-bending element. *Journal of Strain Analysis* 1971; **6**(1):20–24.
27. Dawe DJ. Shell analysis using a simple facet element. *Journal of Strain Analysis* 1972; **7**(4):266–270.
28. Irons BM. The semiloof shell element. *Finite Elements for Thin Shells and Curved Members*. Wiley: New York, 1976; 197–222.
29. Nagtegaal JC, Slater JG. A simple non-compatible thin shell element based on discrete Kirchhoff theory. *Nonlinear Finite Element Analysis of Plates and Shells* (ASME, AMD) 1981; **48**:167–192.
30. Crisfield MA, Tan D. Large-strain elasto-plastic shell analysis using low-order elements. *Engineering Computations* 2001; **18**:255–285.
31. Areias PMA, Belytschko T. Non-linear analysis of shells with arbitrary evolving cracks using xfem. *International Journal for Numerical Methods in Engineering* 2005; **62**:384–415.
32. Peng X, Crisfield MA. A consistent co-rotational formulation for shells using the constant stress/constant moment triangle. *International Journal for Numerical Methods in Engineering* 1992; **35**:1829–1847.

33. Kolahi AS, Crisfield MA. A large-strain elasto-plastic shell formulation using the Morley triangle. *International Journal for Numerical Methods in Engineering* 2001; **52**:829–849.
34. Batoz JL, Zheng CL, Hammadi F. Formulation and evaluation of new triangular, quadrilateral, pentagonal and hexagonal discrete Kirchhoff plate/shell elements. *International Journal for Numerical Methods in Engineering* 2001; **52**:615–630.
35. Crisfield MA, Tan D. Rotation shape functions for a low-order quadrilateral plate element with mid-side rotations. *Communications in Numerical Methods in Engineering* 2001; **17**:191–199.
36. Antman SS, Marlow RS. Material constraints, Lagrange multipliers, and compatibility, applications to rod and shell theories. *Archives for Rational Mechanics and Analysis* 1991; **116**:257–299.
37. Naghdi PM. *Progress in Solid Mechanics*, vol. IV, Chapter—Foundations of Elastic Shell Theory. North-Holland: Amsterdam, 1963; 3–90.
38. Hughes TJR, Carnoy E. Nonlinear finite element shell formulation accounting for large membrane strains. *Computer Methods in Applied Mechanics and Engineering* 1983; **39**:69–82.
39. Bishop RL, Goldberg SI. *Tensor Analysis on Manifolds*. Dover: New York, 1980.
40. Lovelock D, Rund H. *Tensors, Differential Forms and Variational Principles*. Dover: New York, 1989.
41. Fortin M (ed.). *Plates and Shells, CRM Proceedings and Lecture Notes*, vol. 21, CRM Centre de Recherches Mathématiques, Université de Montréal. ASM American Mathematical Society, 1999.
42. Reddy BD, Küssner M. Some low-order quadrilateral elements based on novel integration rules. *Engineering Computations* 1998; **15**(6):700–720.
43. Korelc J, Wriggers P. Consistent gradient formulation for a stable enhanced strain method for large deformation. *Engineering Computations* 1996; **13**(1):103–123.
44. Ibrahimbegović A, Brank B, Courtois P. Stress resultant geometrically exact form of classical shell model and vector-like parameterization of constrained finite rotations. *International Journal for Numerical Methods in Engineering* 2001; **52**:1235–1252.
45. Altmann SL. Hamilton, Rodrigues and the quartenion scandal. *Mathematics Magazine* 1989; **62**(5):291–308.
46. Liu WK, Hu Y-K, Belytschko T. Multiple quadrature underintegrated finite elements. *International Journal for Numerical Methods in Engineering* 1994; **37**:3263–3289.
47. MacNeal RH, Harder RL. A proposed standard set of problems to test finite element accuracy. *Finite Elements in Analysis and Design* 1985; **1**:1–20.
48. Sze KY, Lo SH, Yao L-Q. Hybrid-stress solid elements for shell structures based upon a modified variational functional. *International Journal for Numerical Methods in Engineering* 2002; **53**:2617–2642.
49. Timoshenko S, Woinowsky-Krieger S. *Theory of Plates and Shells* (2nd edn). McGraw-Hill: New York, 1959.
50. Liu WK, Guo Y, Belytschko T. A multiple-quadrature eight-node hexahedral finite element for large deformation elastoplastic analysis. *Computer Methods in Applied Mechanics and Engineering* 1998; **154**: 69–132.
51. Andelfinger U, Ramm E. EAS-elements for two-dimensional, three-dimensional, plate and shell structures and their equivalence to HR-elements. *International Journal for Numerical Methods in Engineering* 1993; **36**:1311–1337.
52. Morley LSD. *Skew Plates and Structures*. International Series of Monographs in Aeronautics and Astronautics. MacMillan: New York, 1963.
53. Bathe K-J, Dvorkin EN. A formulation of general shell elements—the use of mixed interpolation of tensorial components. *International Journal for Numerical Methods in Engineering* 1986; **22**:697–722.
54. Sze KY, Sim YS, Soh AK. A hybrid stress quadrilateral shell element with full rotational D.O.F.S. *International Journal for Numerical Methods in Engineering* 1997; **40**:1785–1800.
55. Parish H. An investigation of a finite rotation four node assumed strain shell element. *International Journal for Numerical Methods in Engineering* 1991; **31**:127–150.
56. Bucalem ML, Bathe K-J. Higher-order MITC general shell elements. *International Journal for Numerical Methods in Engineering* 1993; **36**:3729–3754.
57. Weissman SL. High-accuracy low-order three-dimensional brick elements. *International Journal for Numerical Methods in Engineering* 1996; **39**:2337–2361.
58. Hauptmann R, Schweizerhof K. A systematic development of solid-shell element formulations for linear and non-linear analyzes employing only displacement degrees of freedom. *International Journal for Numerical Methods in Engineering* 1998; **42**:49–69.
59. Kasper EP, Taylor RL. A mixed-enhanced strain method. Part I: geometrically linear problems. *Computers and Structures* 2000; **75**:237–250.

60. Betsch P, Stein E. Numerical implementation of multiplicative elasto-plasticity into assumed strain elements with application to shells at large strains. *Computer Methods in Applied Mechanics and Engineering* 1999; **179**:215–245.
61. Puso MA. A highly efficient enhanced assumed strain physically stabilized hexahedral element. *International Journal for Numerical Methods in Engineering* 2000; **49**:1029–1064.
62. Chen Y-I, Stolarski HK. Extrapolated fields in the formulation of the assumed strain elements. Part II: three-dimensional problems. *Computer Methods in Applied Mechanics and Engineering* 1998; **154**:1–29.
63. Wang TK, Chang CS, van Mier JGM, Sluys LJ, Bittencourt TN. Fracture modeling of concrete using two different microstructural mechanics concepts. *2001 Mechanics and Materials Summer Conference*, University of California, San Diego, 2001. ASME, ASCE, SES.
64. Bathe K-J, Iosilevich A, Chapelle D. An evaluation of the MITC shell elements. *Computers and Structures* 2000; **75**:1–30.
65. Love AEH. *A Treatise on the Mathematical Theory of Elasticity*. Dover: New York, 1996.
66. Betsch P, Menzel A, Stein E. On parametrization of finite rotations in computational mechanics. A classification of concepts with application to smooth shells. *Computer Methods in Applied Mechanics and Engineering* 1998; **155**:273–305.
67. Massin P, Al Mikdad M. Nine node and seven node thick shell elements with large displacements and rotations. *Computers and Structures* 2002; **80**:835–847.
68. Haugen B. Buckling and stability problems for thin shell structures using high performance finite elements. *Ph.D. Thesis*, University of Colorado, Department of Aerospace Engineering, 1994.
69. Sabir AB, Lock AC. The application of finite elements to the large deflection geometrically nonlinear behavior of cylindrical shells. *Variational Methods in Engineering*. University Press: Southampton, 1972; 7/66–7/75.
70. Ramm E. The Riks/Wempner approach—an extension of the displacement control method in nonlinear analyses. *Recent Advances in Non-linear Computational Mechanics*, Chapter 3. Pineridge Press Limited: Swansea, U.K., 1982; 63–86.
71. Oliver J, Oñate E. A total Lagrangian formulation for geometrically nonlinear analysis of structures using finite elements. Part I. Two dimensional problems: shell and plate structures. *International Journal for Numerical Methods in Engineering* 1984; **20**:2253–2281.
72. Sansour C, Bufler H. An exact finite rotation shell theory, its mixed variational formulation and its finite element implementation. *International Journal for Numerical Methods in Engineering* 1992; **34**:73–115.
73. Hibbitt, Karlsson, Sorensen. *Abaqus/Standard Example Problems Manual*, *volumes I and II* (5.7 edn), 1997.
74. Arregui I, Destuynder P, Salaun M. An Eulerian approach for large displacements of thin shells including geometric non-linearities. *Computer Methods in Applied Mechanics and Engineering* 1997; **140**:361–381.
75. Cho C, Park HC, Lee SW. Stability analysis using a geometrically nonlinear assumed strain solid shell element model. *Finite Elements in Analysis and Design* 1998; **29**:121–135.
76. Eriksson A, Pacoste C. Element formulation and numerical techniques for stability problems in shells. *Computer Methods in Applied Mechanics and Engineering* 2002; **191**:3775–3810.
77. Nour-Omid B, Rankin CC. Finite rotation analysis and consistent linearization using projectors. *Computer Methods in Applied Mechanics and Engineering* 1991; **93**:353–384.
78. Stander N, Matzenmiller A, Ramm E. An assessment of assumed strain methods in finite rotation shell analysis. *Engineering Computations* 1989; **6**:58–65.
79. Crisfield MA, Peng X. Instabilities induced by coarse meshes for a nonlinear shell problem. *Engineering Computations* 1996; **13**(6):110–114.
80. Lee WJ, Lee BC. An effective finite rotation formulation for geometrical non-linear shell structures. *Computational Mechanics* 2001; **27**:360–368.
81. Brank B, Ibrahimbegovic A. On the relation between different parametrizations of finite rotations for shells. *Engineering Computations* 2001; **18**:950–973.
82. Basar Y, Ding Y. Finite rotation shell elements for the analysis of finite rotation shell problems. *International Journal for Numerical Methods in Engineering* 1992; **34**:165–169.
83. Buechter N, Ramm E. Shell theory versus degeneration—a comparison in large rotation finite element analysis. *International Journal for Numerical Methods in Engineering* 1992; **34**:39–59.
84. Sansour C, Bocko J. On hybrid stress, hybrid strain and enhanced strain finite element formulations for a geometrically exact shell theory with drilling degrees of freedom. *International Journal for Numerical Methods in Engineering* 1998; **43**:175–192.

85. Li M, Zhan F. The finite deformation theory for beam, plate and shell. Part 5. The shell element with drilling degree of freedom based on biot strain. *Computer Methods in Applied Mechanics and Engineering* 2000; **189**:743–759.
86. Sansour C, Kollmann FG. Families of 4-node and 9-node finite elements for a finite deformation shell theory. An assessment of hybrid stress, hybrid strain and enhanced strain elements. *Computational Mechanics* 2000; **24**:435–447.
87. Masud A, Tham CL, Liu WK. A stabilized 3D co-rotational formulation for geometrically nonlinear analysis of multi-layered composite shells. *Computational Mechanics* 2000; **26**:1–12.
88. Sze KY, Chan WK, Pian THH. An eight-node hybrid-stress solid-shell element for geometric non-linear analysis of elastic shells. *International Journal for Numerical Methods in Engineering* 2002; **55**:853–878.
89. Parish H. A continuum-based shell theory for non-linear applications. *International Journal for Numerical Methods in Engineering* 1995; **38**:1855–1883.
90. Bischoff M, Ramm E. Shear deformable shell elements for large strains and rotations. *International Journal for Numerical Methods in Engineering* 1997; **40**:4427–4449.
91. El-Abbasi N, Meguid SA. A new shell element accounting for through-thickness deformation. *Computer Methods in Applied Mechanics and Engineering* 2000; **189**:841–862.

